International Journal of Mechanical Sciences 259 (2023) 108601

Contents lists available at ScienceDirect

International Journal of Mechanical Sciences

journal homepage: www.elsevier.com/locate/ijmecsci

# Data-driven modelling of the multiaxial yield behaviour of nanoporous metals

Lena Dyckhoff [a,*], Norbert Huber [a,b]

[a] Institute of Materials Mechanics, Helmholtz-Zentrum Hereon, Max–Planck-Straße 1, Geesthacht, 21502, Germany
[b] Institute of Materials Physics and Technology, Hamburg University of Technology, Eißendorfer Straße 42, Hamburg, 21073, Germany

ARTICLE INFO

*Keywords:*
Yield condition
Anisotropic material
Porous material
Finite elements
Machine learning

ABSTRACT

Nanoporous metals, built out of complex ligament networks, can be produced with an additional level of hierarchy. The resulting complexity of the structure makes modelling of the mechanical behaviour computationally expensive and time consuming. In addition, multiaxial stresses occur in the higher hierarchy ligaments. Therefore, knowledge of the multiaxial material behaviour, including the 6D yield surface, is required. Surrogate models, predicting the mechanical behaviour of the lower level of hierarchy, represented by finite element beam models, are a promising approach to overcome such challenges, when existing analytical models are not able to describe the material behaviour. Therefore, as a first step, we studied the elastic behaviour and the yield surfaces of representative volume elements with idealised diamond and Kelvin structure in finite element simulations. The yield surfaces showed pronounced anisotropy and could not be described by the Deshpande-Fleck model for isotropic solid foams. Instead, we used data-driven and hybrid artificial neural networks, as well as data-driven support vector machines and compared them regarding their potential for the prediction of yield surfaces. All considered methods were well suited and resulted in relative errors $< 4.5\,\%$. Support vector machines showed the best generalisation and accuracy in 6D stress space and are suitable for extrapolation outside the range of training data.

## 1. Introduction

Nanoporous metals, exhibiting a complex bicontinuous network of interconnected metallic ligaments and pore space on the nanoscale, are extensively studied with regard to applications in catalysis, actuation and sensing technology [1–3]. Most studies dealing with nanoporous metals focus on nanoporous gold (NPG) to study e.g. small-scale mechanical behaviour [2,4,5]. The nanoporous network of NPG evolves during chemical dealloying, where the choice of process parameters highly influences the microstructure and properties [6,7]. The evolved nanoscale ligaments result in the material's high specific strength [4,8].

By combining multiple dealloying steps, Shi et al. [7] were able to integrate a porous network into the ligaments and, as such, another level of hierarchy. This modification results in even smaller length scales and, thus, higher strength for constant relative density [7]. However, the material's mechanical properties, including Young's modulus, Poisson's ratio and yield stress, depend on further parameters such as ligament size and geometry [9,10], connectivity [11], relative density [12,13], ligament orientation [14] and curvature [9]. The statistical distribution of each of these descriptors additionally influences the macroscopic properties [15]. Experimental analysis of the relationship between these parameters and the resulting mechanical properties requires an extensive sample preparation and in-depth microstructural analysis, which is a challenging and time consuming task, in particular when more than one level of hierarchy is involved.

Modelling, especially finite element (FE) modelling, is a very beneficial tool to support experimental studies and to obtain a deeper understanding of the deformation mechanisms. To model foams and describe their mechanical properties depending on structural parameters such as solid fraction, ideal periodic beam-like structures, e.g. the well-known Gibson-Ashby structure [16], are commonly used. Analysing relationships between topology and resulting mechanical properties have been focus of numerous publications [17–21].

A review of experimentally informed modelling methods for the characterisation of nanoporous metals can be found in [5]. NPG shows a local coordination of the ligaments of 3 or 4, which makes 4-coordinated structures such as the diamond cell suitable as a basis for modelling NPG [12]. Using idealised 4-coordinated structures is beneficial, because it also allows modelling of 3-coordinated structures by cutting ligaments and achieving more realistic structures by random

* Corresponding author.
*E-mail address:* lena.dyckhoff@hereon.de (L. Dyckhoff).

https://doi.org/10.1016/j.ijmecsci.2023.108601
Received 31 January 2023; Received in revised form 3 July 2023; Accepted 3 July 2023
Available online 6 July 2023

displacements of the nodes [12,22]. Another 4-coordinated cell is the Kelvin cell, which is a space-filling, 14-sided well-studied polyhedron and commonly used to model open-cell polymer foams [23–25].

Highly efficient FE-beam models, which are used in this work, were developed to describe the mechanical behaviour of NPG [9,10,12,26–30]. These were first based on diamond cells [12] and later improved for model reconstruction from tomographic data [10,28]. Even though beam models represent a significant simplification of the solid models, it is possible to achieve a comparable macroscopic mechanical response by implementing a nodal correction [29].

In previous experimental studies on NPG, the mechanical behaviour under uniaxial loading was analysed [4,8,31]. The behaviour under multiaxial loading, however, is still mostly untouched and, in addition, not accessible through experiments. Mangipudi et al. [32] used simulations with FE-models from tomographic reconstruction to study the plastic Poisson's ratio. Thereby, they found disagreement between the resulting 2D yield loci and the Deshpande-Fleck model for isotropic solid foams [33] under axisymmetric and plane stress load conditions. However, for hierarchical NPG, multiaxial loading becomes an essential issue, because the structural elements of the lower level of hierarchy are exposed to the multiaxial stresses originating from the higher level of hierarchy. On the latter, these arise from combined axial tension/compression, bending and torsion of the ligaments as well as inhomogeneous stress fields in the transition regions from ligaments to nodes [9,14]. Modelling of the mechanical response of the lower level of hierarchy, therefore, requires the knowledge of the multiaxial yield surface in 6D stress space.

For macroscopic solid foams, common formulations of the yield condition include the Deshpande-Fleck model [33] or the Miller criterion [34]. These are often not able to describe materials with complex structure and anisotropic behaviour. Liu et al. [35] combined the Drucker–Prager [36] and Hill [37] criterion to include anisotropy for orthotropic materials as well as asymmetry in uniaxial tension and compression. However, the Drucker–Prager criterion does not include finite yield stresses under hydrostatic compression. Furthermore, these models do not include relationships regarding geometrical and structural parameters, which are important in nanoporous metals [15,21,26–28]. Here, machine learning (ML) is a tool, which is able to find complex, non-linear relationships between a variety of features and required output variables. Such techniques experience a strong upwards trend in different fields, including applications in materials science and mechanical engineering [38–40].

In this article, we focus on ML techniques for the prediction and evaluation of yield surfaces and plasticity. Various studies exist on this topic, of which a selection is summarised in the following. Ibáñez et al. [41] implemented a hybrid approach to correct existing constitutive yield equations such as Barlat's or Hill's model with regard to observed experimental data by using the sparse proper generalised decomposition algorithm. Another hybrid approach proposed by Frankel et al. [42] uses a combination of the Danielsson model with artificial neural networks (ANNs) or Gaussian Process Regression to model elastomeric constitutive laws of bcc-structures. Heidenreich et al. [43] uses fully-connected neural networks to predict yield surfaces based on microstructure of porous media extracted from images by convolutional neural networks. ANNs were used by Shen et al. [44] for the prediction of yield surfaces depending on the porosity of 2D porous materials. A hybrid multiscale neural network approach combining ANNs with established physics-based laws in plasticity was proposed by Settgast et al. [45] to predict the elastic–plastic response of a 2D open-cell foam. This approach was further developed with regard to a 3D open-cell Wheire-Phelan structure by Malik et al. [46]. Convex artificial neural networks were suggested by Fuhg et al. [47] for the description of crystal plasticity. Park et al. [48] used molecular dynamics and symbolic regression, to obtain a functional description of yield surfaces of polymers under multiaxial loading depending on the load history. Recurrent neural networks [49–51] and mechanistically informed ANNs [52] were suggested to describe path-dependent plasticity. Symbolic regression, combined with micromechanical FE simulations, was used by Bomarito et al. [53] to describe plasticity in an interpretable manner as yield equations. Hartmaier [54] suggested to describe the yield surface of a Hill-like material via support vector classification (SVC) and demonstrated its application in FE analysis for 3D stress space. This approach was extended to 6D stress space by Shoghi et al. [55]. In contrast to the previous mainly supervised approaches, Flaschel et al. [56] propose the unsupervised learning approach EUCLID to describe plasticity based on forces and displacements instead of stresses and strains.

The majority of the mentioned studies considered only 2D to 3D loading/models or incompressible materials. In the present study, we aim to study not only a single approach, but compare the applicability of different, predominantly data-driven approaches, for the prediction of yield surfaces in 6D stress space for nanoporous metals i.e. open-cell foams. Furthermore we are introducing a hybrid approach based on the Deshpande-Fleck model for isotropic solid foams [33]. Therefore, first, an overview is given on the applied methods and theories. This is followed by an analysis of the elastic response of FE-beam models with diamond and Kelvin architecture in Section 3. The elastic–plastic response under uniform, multiaxial loading is discussed in Section 4 with focus on the description of yield surfaces in 3D and 6D stress space. The Deshpande-Fleck model for isotropic solid foams [33] and the ML algorithms, including approaches using ANNs and SVCs, are discussed in the scope of their applicability for the prediction of the thus generated yield surfaces in Section 5. This study will form the basis for future development of a surrogate model, which will be able to describe the mechanical behaviour of the nanoporous network on the lower level of hierarchy in hierarchical nanoporous metals.

## 2. Methods

In this work, the elastic–plastic deformation behaviour under multiaxial loading conditions of open-pore structures with diamond and Kelvin architecture are studied using load controlled FE simulations with Abaqus [57]. In this section, a description of the FE models and the elastic–plastic material behaviour based on continuum mechanics, including the Deshpande-Fleck model for isotropic solid foams, is given. The data generated with FE simulations will be used for training and testing of machine learning methods. Methods for the prediction of yield surfaces – ANN, SVC and a hybrid model using ANNs – will be introduced in Section 2.4.

### 2.1. Finite-element modelling for data generation

FE simulations are conducted on representative volume elements (RVEs). For simplicity and because of their different characteristics of anisotropy, see [19,58] and Fig. 1(c) and (d), a diamond and a Kelvin cell of unit length and volume are used as RVE, see Fig. 1(a) and (b). The RVEs are built out of cylindrical ligaments, each consisting of 10 beam elements of type B31 (beam in space) with circular cross section. Two elements at each end of the ligament, i.e. 4 elements per ligament, were used to implement the node correction proposed by Odermatt et al. [29], which results in larger radii in the nodal areas in Fig. 1(a) and (b). This node correction ensures that the effective elastic–plastic behaviour of the FE-beam model matches that of the corresponding FE solid model. The geometrical parameters and material properties assigned to elements with and without node correction are summarised in Table 1.

Periodic boundary conditions, which also consider rotational degrees of freedom (DOF), due to the FE-beam elements used for the spacial discretisation of the ligaments, are applied to both RVEs [10,28]. To this end, reference nodes (e.g. "SET-DUMMY-X") are defined in the centre of the three faces with non-zero normal coordinates ($x = 1$, $y = 1$, $z = 1$), black solid circles in Fig. 1(a) and (b). These are linearly

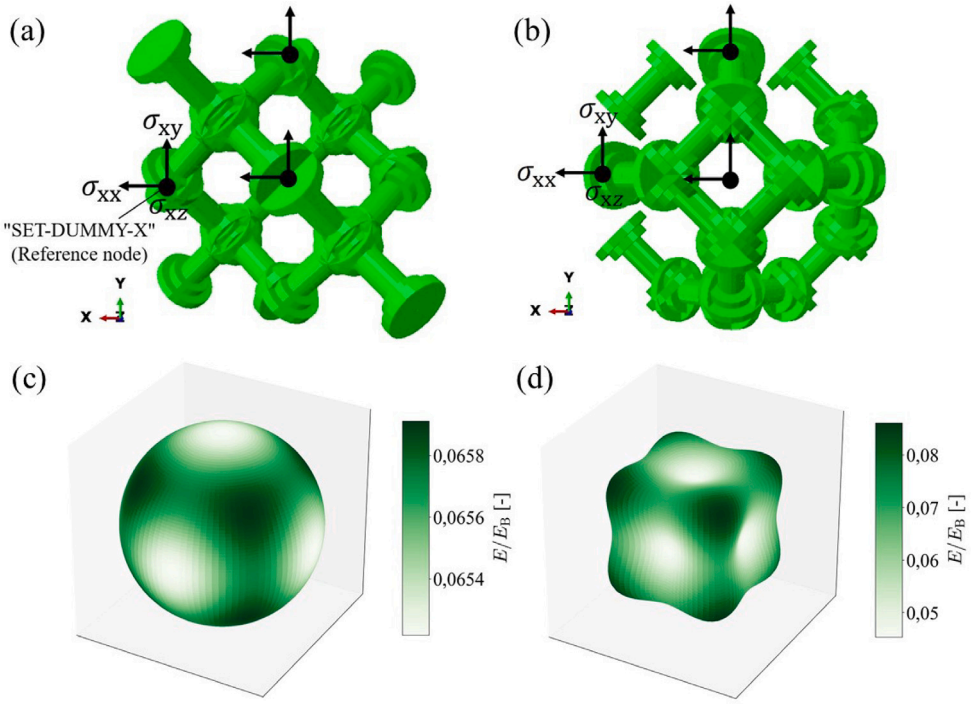


**Fig. 1.** RVEs with (a) diamond and (b) Kelvin structure. The reference nodes, where loads are applied, are designated as black solid circles (e.g. "SET-DUMMY-X" in (a)). The anisotropy, in form of the direction dependent Young's modulus $E$ normalised to the Young's modulus of the bulk material $E_B$ (see Section 3), is shown for the (c) diamond and (d) Kelvin RVE.

**Table 1**
Parameters for the RVEs used in FE simulations shown in Fig. 1. The upper part includes geometrical parameters and the lower part material properties of the elements. 'B' refers to elements with properties of bulk gold and 'NC' to the elements used for the node correction.

| Parameter | Variable | Unit | Diamond | Kelvin |
|---|---|---|---|---|
| Cell size | $a$ | mm | 1 | 1 |
| Elements/ligament | $n_{elem/lig}$ | – | 10 | 10 |
| Elements NC/ligament | $n_{NC}$ | – | 4 | 4 |
| Nominal ligament length | $l/a$ | – | $\sqrt{3}/4$ | $\sqrt{2}/4$ |
| Nominal ligament radius | $r/a$ | – | 0.1221 | 0.1119 |
| Radius NC 1st element | $r_{NC1}/a$ | – | 0.2020 | 0.1952 |
| Radius NC 2nd element | $r_{NC2}/a$ | – | 0.2820 | 0.2785 |
| Young's modulus | $E_B$ | GPa | 80 | 80 |
| Poisson's ratio | $\nu_B$ | – | 0.42 | 0.42 |
| Hardening rate | $E_{T,B}$ | GPa | 6 | 6 |
| Hardening rate NC | $E_{T,NC}$ | GPa | 1.4 | 1.1 |
| Yield stress | $\sigma_{Y,B}$ | MPa | 200 | 200 |
| Yield stress NC | $\sigma_{Y,NC}$ | MPa | 47 | 37 |

coupled to the relative deformations of the junction nodes in opposite faces by defining e.g.

$$u_x^0 - u_x^1 + u_x^{Ref} = 0 \quad \Rightarrow$$

NSETX0, 1, 1, NSETX1, 1, −1, SET-DUMMY-X, 1, 1

as equations in Abaqus, where $u_x^1$ and $u_x^0$ are the deformations in $x$-direction of the nodes in the node sets (NSETX1 and NSETX0) in the face with $x = 1$ and $x = 0$, respectively. $u_x^{Ref}$ is the deformation of the reference node and corresponds to the resulting, homogenised relative deformation of the RVE, which is used to calculate the strains. The reference nodes are further used to apply the multiaxial loads for the load controlled simulations. The rotational DOF of the node sets in opposite faces are linearly coupled and the boundary conditions for rotational DOF are chosen such that rigid body rotations are prevented under shear loads. The RVEs are generated using Python scripting, which, for the diamond RVE, was described in more detail in previous works [10,12]. The Kelvin RVE is built in a similar manner, except that elements of ligaments in opposite faces occur only one-sided, see Fig. 1(b), preventing their duplication and an overestimation of the RVEs stiffness, when using periodic boundary conditions.

The nominal ligament radii $r/a$, Table 1, are iteratively determined such that the solid fraction $\varphi$ is approximately 26.35%, which is in accordance with experiments [4,12]. Furthermore, constant solid fractions allow a better comparison of the results of the two RVEs considered in this work and with the Young's modulus of a solid model by Richert et al. [10] with similar geometry. For the diamond RVE, the determined radius is 2.4% smaller than the one used in [10], due to approximations in the analytic calculation of the solid fractions $\varphi_D$ and $\varphi_K$ given by

$$\varphi_D = 16V_C - 8V_S = 16\pi r^2\left(l - \frac{2}{3}r\right) \quad (1)$$

$$\varphi_K = 24V_C - 12V_S = 24\pi r^2\left(l - \frac{2}{3}r\right) \quad (2)$$

for the diamond and Kelvin RVE, respectively. The RVE specific ligament lengths $l/a$ are given in Table 1. The volume of each cylindrical ligament and spherical node was approximated to $V_C = \pi r^2 l$ and $V_S = 4/3\pi r^3$, respectively. One half sphere was subtracted from the volume per each end of a ligament, due to the overlap of ligaments and spherical nodes.

Gradually increasing radii in the nodal area, which are shown in Fig. 1(a) and (b) and are given as $r_{NC1}/a$ and $r_{NC2}/a$ in Table 1, are solely used for the stiffness correction of the otherwise too soft nodes in the beam model. This makes the beam models comparable to a solid model with same solid fraction and cylindrical ligament shape [29]. Thus, cylindrical ligaments and identical radii in nodes and ligaments are assumed for the calculation of the solid fraction.

The material behaviour assigned to each of the beam elements follows

$$d\sigma_{\mathrm{B}} = \begin{cases} E_{\mathrm{B}} d\epsilon_{\mathrm{el}} & \sigma < \sigma_{\mathrm{Y,B}} \\ E_{\mathrm{T,B}} d\epsilon_{\mathrm{pl}} & \sigma \geq \sigma_{\mathrm{Y,B}}. \end{cases} \tag{3}$$

and is thus described by a linear elastic region followed by a plastic region with linear isotropic hardening. The material parameters assigned to the elements are those of gold and given in Table 1. Therein, the subscript 'B' denotes the mechanical properties of the 'bulk' gold phase and 'NC' refers to the properties for the elements in the nodal areas.

### 2.2. Mechanical modelling of solid foams

Due to the underlying elastic–plastic material response on the microscale, i.e. in the metal ligaments making up the open pore nanofoam, the macroscopic behaviour is elastic–plastic as well. In general, the response to applied loads in the linear elastic regime follows Hooke's law of linear elasticity [59]

$$\mathbf{E} = \mathscr{S}\mathbf{T} \tag{4}$$

with strain tensor $\mathbf{E}$ with components $\epsilon_{ij}$, predefined stress tensor $\mathbf{T}$ with components $\sigma_{ij}$ as well as and compliance tensor $\mathscr{S}$ of 4th order with components $S_{ijkl}$. The components $S_{ijkl}$ are defined by the elastic material properties Young's modulus $E$, Poisson's ratio $\nu$ and shear modulus $G$. The anisotropy of a structure in the elastic regime can be quantified by

$$A = G/G_{\mathrm{iso}}. \tag{5}$$

where $G$ is its shear modulus and $G_{\mathrm{iso}}$ the shear modulus for isotropic materials defined by

$$G_{\mathrm{iso}} = \frac{E}{2(1+\nu)}. \tag{6}$$

For further load increase beyond the onset of plastic yielding, a nonlinear plastic region is expected to follow the linear elastic regime, modelled by Eq. (4). Plasticity can result in large deformations and strains, leading to changes in the areas during deformation of the RVE. For large deformations, this influences the yield stress, see Fig. 2, and, thus, the asymmetry and anisotropy of the yield surface. Furthermore, considering the true geometries of the RVE is of importance, if combined normal and shear loads are analysed, which will be discussed in Section 4.3. Hence, in this work, yield stresses are defined from true Cauchy stresses $\mathbf{T}$ and true logarithmic strains $\mathbf{E}$. These are determined via

$$\mathbf{E} = \frac{1}{2}\ln\left(\mathbf{F}^{\mathrm{T}}\mathbf{F}\right) \qquad \text{and} \qquad \mathbf{T} = \frac{1}{|\det\mathbf{F}|}\mathbf{T}_0\mathbf{F}^{T} \tag{7}$$

with the first Piola–Kirchhoff stress tensor $\mathbf{T}_0$ and deformation gradient $\mathbf{F}$ [59,60].

To define the onset of plastic yielding under multiaxial load conditions, equivalent stresses and strains are defined and compared to a critical stress value in a yield criterion. A common yield criterion for metals is the von Mises yield criterion with the von Mises equivalent stress

$$\sigma_e = \sqrt{\frac{3}{2}\sigma'_{ij}\sigma'_{ij}} \tag{8}$$

with components $\sigma_{ij}$ of the stress tensor $\mathbf{T}$, deviatoric stresses

$$\sigma'_{ij} = \sigma_{ij} - \sigma_m\delta_{ij} \tag{9}$$

and hydrostatic mean stress

$$\sigma_m = \sigma_{kk}/3. \tag{10}$$

Volume conservation and isotropy are usually assumed for plastic deformation of materials that follow the von Mises yield criterion in connection with an associated flow rule, which makes it independent of the hydrostatic part of the stress tensor. Nanoporous metals are highly compressible [4]. Therefore, in our case, plastic yielding under hydrostatic loading must be considered. Hence, equivalent stresses and strains are defined as the Frobenius norm of the stress and strain tensors

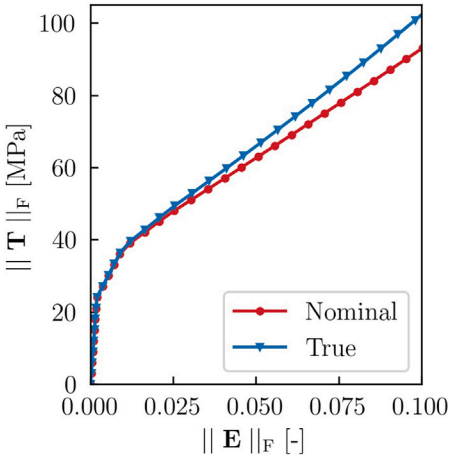


**Fig. 2.** Stress–strain curves for hydrostatic loading determined from first Piola–Kirchhoff stress and linearised strain (nominal) as well as Cauchy stresses and logarithmic strains (true).

$$\|\mathbf{T}\|_{\mathrm{F}} = \sqrt{\sigma_{ij}\sigma_{ij}} \qquad \text{and} \qquad \|\mathbf{E}\|_{\mathrm{F}} = \sqrt{\epsilon_{ij}\epsilon_{ij}}. \tag{11}$$

Thus, yield stresses are not projected to the plane of deviatoric stresses, as is the case for common measures of equivalent stresses and strains.

Existing models for the description of yield surfaces of solid foams include the Drucker–Prager yield criterion and its extensions e.g. Miller [34] or Deshpande-Fleck [33] yield criterion, which have varying complexity with regard to the amount of necessary description parameters. Furthermore, these models are all described by the first invariant of the stress tensor, Eq. (10), and the second deviatoric invariant, Eq. (8), and include the classical von Mises yield criterion as a special case. In the following, we will use the Deshpande-Fleck model for isotropic solid foams, because it is used in literature to describe the yield behaviour of nanoporous gold [31,32].

For modelling, not only the initial yield surface but also its evolution during plastic deformation is of importance. This increases the complexity of the modelling of anisotropic deformation behaviour significantly. As a first step in this direction, the yield stresses in this work are defined at 1 and 10% plastic strain from FE simulation data. In elastic and plastic calculations the first Piola–Kirchhoff stress tensor is defined by the predefined forces. The resulting deformations of the RVE are determined at the reference points and used to define the deformation gradient of the RVE. Strain tensor and Cauchy stress tensor are determined using this deformation gradient, see Eq. (7). The tensors are reduced to the Frobenius norm, Eq. (11), to determine the yield stresses by evaluating the resulting stress–strain relationship, similar to common uniaxial load cases.

#### 2.2.1. Deshpande-Fleck model for isotropic solid foams

As will be shown in Section 4, the yield surfaces of the considered diamond and Kelvin RVEs are anisotropic. Nonetheless, the Deshpande-Fleck model for isotropic solid foams [33] is used as a first approximation of the yield stresses of the FE-beam models, as a benchmark for the ML approaches and as a starting point for the hybrid ML approach (see Section 2.4.2), due to its simplicity. Additionally, real samples of NPG are expected to show a more isotropic behaviour, at least for radial loading processes.

The model uses the invariants mean stress $\sigma_{\mathrm{m}}$, Eq. (10), and effective stress $\sigma_{\mathrm{e}}$, Eq. (8), together with a parameter $\alpha$, in the following denoted

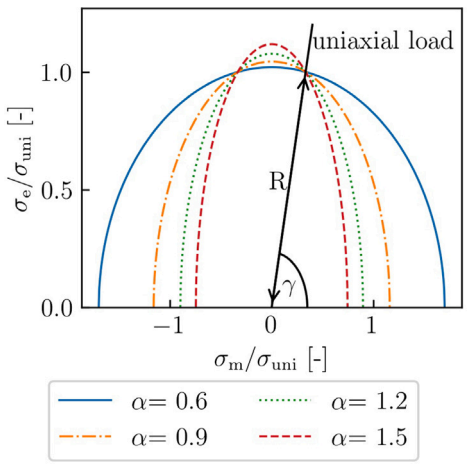


**Fig. 3.** Deshpande-Fleck yield surfaces in space of mean ($\sigma_m$) and von Mises equivalent ($\sigma_e$) stress normalised to the yield stress under uniaxial compression ($\sigma_{uni}$). The parameter $\alpha$ is varied in the range [0.6, 1.5] and the introduced polar coordinates $R$ and $\gamma$ are indicated for the line corresponding to uniaxial loading.

as ellipticity parameter, to define the equivalent stress

$$\hat{\sigma}^2 \equiv \frac{1}{\left[1+(\alpha/3)^2\right]}\left(\sigma_e^2+\alpha^2\sigma_m^2\right), \tag{12}$$

which is compared to the yield stress under uniaxial compression $\sigma_{uni}$, as it is accessible through experiments with mm-sized samples of NPG [7,8]. The yield criterion $F=\hat{\sigma}-\sigma_{uni}=0$ then leads to the yield function

$$\sigma_e=\sqrt{\left[1+(\alpha/3)^2\right]\sigma_{uni}^2-\alpha^2\sigma_m^2} \tag{13}$$

in the space of mean and effective stress.

The only parameter necessary to fit the model to experimental or simulation data is

$$\alpha=\sqrt{\left[\left(\sigma_{hyd,m}/\sigma_{uni}\right)^2-1/9\right]^{-1}} \tag{14}$$

with mean hydrostatic yield stress $\sigma_{hyd,m}=\sigma_{hyd}/\sqrt{3}$, where $\sigma_{hyd}$ is the yield stress under hydrostatic compression [33]. $\sigma_{uni}$ and $\sigma_{hyd}$ are determined from FE simulations. Fig. 3 shows the influence of the ellipticity parameter $\alpha$ on the shape of the yield function. It gets clear that the yield stress increases for hydrostatic loading with decreasing $\alpha$, while it decreases for non-hydrostatic load cases, reaching von Mises plasticity for $\alpha$ near zero.

To compare the yield stresses from simulation data and prediction by the Deshpande-Fleck yield function in $\sigma_m-\sigma_e$-space, the point of the yield function that belongs to the same direction of multiaxial loading, as it was applied for the simulation, must be defined. This is the case, when the triaxiality factor $\sigma_e/\sigma_m$ is constant. Relating to that, we introduce the polar coordinates $\gamma$ and $R$, depicted in Fig. 3, to describe the points on the yield surface. The angle

$$\gamma=\tan^{-1}\left(\sigma_e/\sigma_m\right), \tag{15}$$

relative to the $\sigma_m$-axis, defines the line with constant triaxiality starting at $\sigma_e=\sigma_m=0$. Each point on that line is defined by the radial component

$$R=\sqrt{\sigma_m^2+\sigma_e^2}, \tag{16}$$

in the following referred to as radius. The difference in radius is of importance in the hybrid approach, which is introduced in Section 2.4.2.

Using the predefined load cases (first Piola–Kirchhoff stress tensors) of the points on the simulated yield surface, $\gamma$ can be defined from Eqs. (8), (10) and (15). Describing $\sigma_m$ as a function of $\gamma$ leads to

$$\sigma_m=\sqrt{\frac{1+(\alpha/3)^2}{\tan^2\gamma+\alpha^2}\sigma_{uni}^2}, \tag{17}$$

which, together with $\sigma_e$, Eq. (13), describes the point on the yield function that corresponds to the same direction of multiaxial loading as it was applied in FE simulations. Knowledge of $\sigma_e$ and $\sigma_m$ allows the calculation of the yield stress

$$\sigma_Y=\sqrt{\frac{2}{3}\left[\sigma_e^2+\frac{1}{2}\left(3\sigma_m\right)^2\right]}, \tag{18}$$

by rearranging Eqs. (8) and (10) such that $\sigma_Y$ is defined from the non-deviatoric stress tensor as in Eq. (11).

### 2.3. Stress vectors in 6D stress space

For larger parameter spaces and when a few representative points are necessary to describe a parameter space, randomly chosen points in space can be very helpful. We chose randomly instead of uniformly distributed points as in [55], because it does not require knowledge of the amount of data necessary for training prior to the training procedure. Pseudo-random numbers are used to distribute vectors on a surface of a multidimensional sphere. Therefore, the method proposed by Muller [61] was applied, for which the n coordinates of a point in nD stress space are drawn from a standard normal distribution and are normalised to the predefined equivalent stress of 150 MPa. The components of the thus generated stress vector are transferred to the stress tensor by adjusting the shear components by a factor of $1/\sqrt{2}$ such that

$$\begin{pmatrix}\sigma_1\\ \sigma_2\\ \sigma_3\\ \sigma_4\\ \sigma_5\\ \sigma_6\end{pmatrix}=\begin{pmatrix}\sigma_{xx}\\ \sigma_{yy}\\ \sigma_{zz}\\ \sqrt{2}\sigma_{xy}\\ \sqrt{2}\sigma_{xz}\\ \sqrt{2}\sigma_{yz}\end{pmatrix}\rightarrow\begin{pmatrix}\sigma_{xx} & \sigma_{xy} & \sigma_{xz}\\ \sigma_{yx} & \sigma_{yy} & \sigma_{yz}\\ \sigma_{zx} & \sigma_{zy} & \sigma_{zz}\end{pmatrix}. \tag{19}$$

This ensures that the stress tensor and, therefore, also the applied loads have the same norm as the defined stress vector. The components of these vectors are used as loading conditions in FE simulations and are part of the input features for ML.

### 2.4. Machine learning techniques

Determining yield surfaces from simulation or experimental data can be very time consuming and in the latter case very challenging, especially regarding multiaxial loading. Thus, in the following, three ML methods are presented, which are used in this work to predict yield surfaces in 6D stress space as a function of the applied multiaxial loads, provided in form of the normalised initial first Piola–Kirchhoff stress tensor.

#### 2.4.1. Data-driven and hybrid artificial neural networks

The first two ML approaches for yield stress prediction use ANNs, implemented in form of multilayer perceptron (MLP) regressors from the scikit-learn python package [62,63]. In the following, the more general term ANNs will be used also for MLPs. The input layer is defined by a vector of features, which, in our case, includes the normalised 3D/6D (normalised) stress vector, Eq. (19), the plastic strain at which the yield stress was determined and the type of structure of the RVE. All of these input features affect the yield stress, which is the target parameter for all approaches. The data-driven approach directly predicts the normalised yield stress ($\sigma_Y/\sigma_{uni}$) as output variable. The yield stress under uniaxial loading $\sigma_{uni}$ of the RVEs for the considered plastic strains was used for normalisation, as it is also used in the Deshpande-Fleck model and can be determined from experiments and

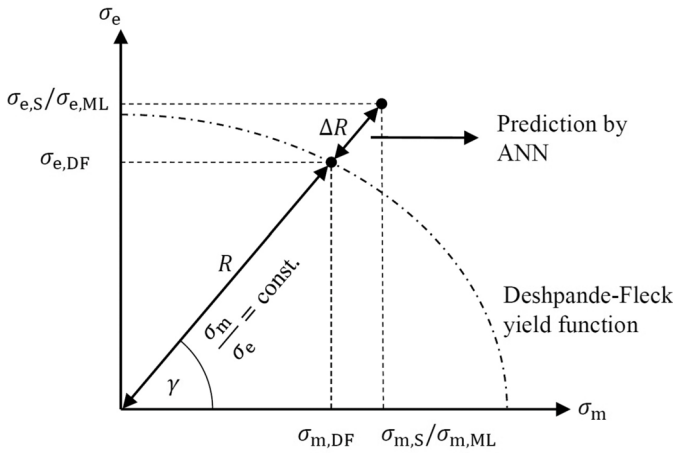


**Fig. 4.** The points on the yield surfaces can either be described by the effective stress $\sigma_e$ and mean hydrostatic stress $\sigma_m$ or by the polar coordinates $R$ and $\gamma$. Deviations of the simulation data ('S') from the Deshpande-Fleck predictions ('DF') are defined by the difference in radius $\Delta R$ and corrected by an ANN. Corrected values are denoted by 'ML'.

simulations. Furthermore, the ratio represents the anisotropy of the yield surface relative to the uniaxial yield stress.

For ANNs, a variety of parameters have to be adjusted to achieve best results and generalisation. This includes the architecture of the ANN, the type of activation function (e.g. sigmoid, tanh or ReLU), solver for weight optimisation (e.g. L-BFGS, Adam or SGD) as well as the parameter $\lambda$ for L2 regularisation. The results of the optimisation procedure are discussed in .

#### 2.4.2. The hybrid model

The hybrid model uses similar ANNs as the data-driven model. However, instead of the yield stress, the output parameter is a correction of the Deshpande-Fleck model, described in Section 2.2.1. We choose the scaled difference in radius $\Delta R/\sigma_{uni}$, schematically shown in Fig. 4, as a correction parameter. $\Delta R$ is defined as

$$\Delta R = R_S - R_{DF} = \sqrt{\sigma_{m,S}^2 + \sigma_{e,S}^2} - \sqrt{\sigma_{m,DF}^2 + \sigma_{e,DF}^2} \tag{20}$$

with radius $R$, Eq. (16), and mean $\sigma_{m,S}$ ($\sigma_{m,DF}$) and effective stress $\sigma_{e,S}$ ($\sigma_{e,DF}$) at the yield point. The subscripts 'S' and 'DF' refer to values from simulation and the Deshpande-Fleck model, respectively.

For training, $\sigma_{m,S}$ and $\sigma_{e,S}$ are calculated from the normalised initial (nominal) stress tensor scaled to the yield stress from simulation data at 1 and 10% plastic strain via Eqs. (8) and (10). We use the yield stress determined from true equivalent stresses and strains, Eq. (11), to include the pronounced anisotropy. The point of the Deshpande-Fleck yield function, given by $\sigma_{m,DF}$, Eq. (17), and $\sigma_{e,DF}$, Eq. (13), for the similar load case, i.e. constant $\gamma$, is determined according to the procedure in Section 2.2.1. With this, $\Delta R$ can be calculated for the training data. For predictions of the yield stresses, first, the point of the Deshpande-Fleck yield function is determined from the stress vector given in the input features, see Eq. (19). Therefore, $\gamma$ is calculated via Eqs. (8), (10) and (15). The parameter $\alpha$ is known from training such that $\sigma_{m,DF}$ and $\sigma_{e,DF}$ are determined with $\gamma$ and $\alpha$ in analogy to the training procedure and result in the radius $R_{DF}$. This radius is then adjusted by the correction parameter $\Delta R$, predicted by the ANN, as shown in Fig. 4. The projection of the corrected radius $R_{ML} = R_{DF} + \Delta R$ to the axes leads to

$$\sigma_{m,ML} = R_{ML}\cos(\gamma) \qquad \text{and} \qquad \sigma_{e,ML} = R_{ML}\sin(\gamma) \tag{21}$$

and, thus, by Eq. (18), to the corrected yield stress $\sigma_{Y,ML}$. In the best case, $\sigma_{Y,ML}$ should agree with the yield stress $\sigma_{Y,S}$, determined for the same load case from stress–strain curves based on simulation data, for any direction of applied stress in 3D or 6D stress space.

#### 2.4.3. Support vector classification

Hartmaier [54] and Shoghi et al. [55] demonstrated that SVC can be applied for prediction of yield stresses for general 3D and 6D load cases for materials with Hill and Barlat-type anisotropy. This shows the potential of the method to represent yield surfaces for general cases of anisotropy. Therefore, SVC, provided by the scikit-learn python package [62,63], was chosen as an additional approach in this work to assign elastic or plastic material behaviour to a given stress state and to determine yield stresses for arbitrary 6D load cases.

During training of SVC, a hyperplane in feature space is calculated, which is the decision boundary for the classification. It is defined by the support vectors (SV) $\mathbf{x}_i$, which are the training data points closest to this hyperplane. The hyperplane is defined such that it has the largest distance to these SV, while providing the smallest error for predictions. The class of a given sample $\mathbf{x}$ is determined by the sign of the decision function

$$f(\mathbf{x}) = \sum_{i \in SV} y_i \alpha_i K(\mathbf{x}_i, \mathbf{x}) + b. \tag{22}$$

$K$ is the kernel function, here radial basis function (RBF)

$$K = \exp(-\gamma \|\mathbf{x} - \mathbf{x}_i\|^2), \tag{23}$$

which allows for mapping of the data into higher dimensions to be able to handle also non-linear problems [62–64]. $y_i\alpha_i$, $b$ and $\gamma$ are parameters determined by the SVC algorithm during the training procedure. For the given problem, $f(\mathbf{x}) < 0$ assigns points to the elastic regime and $f(\mathbf{x}) \geq 0$ to the plastic regime. Thus, SVCs give a data-driven description of the yield surface [54]. The derivative of the decision function

$$\frac{\partial f(\mathbf{x})}{\partial \mathbf{x}} = \sum_{i \in SV} y_i \alpha_i \frac{\partial K(\mathbf{x}_i, \mathbf{x})}{\partial \mathbf{x}} \tag{24}$$

gives a data-driven formulation of the gradient on the yield surface, which can be used in common flow rules and allows a straight forward implementation into FE software [54].

The sampling of data points, defining the elastic ($\|\mathbf{T}\|_F < \sigma_Y$) or elastic–plastic deformation regime ($\|\mathbf{T}\|_F \geq \sigma_Y$), is very important to achieve a good representation of the whole stress space and the yield surface [54]. To ensure that the hyperplane is properly defined by the training data, in this work, besides the usual hyperparameters C and $\mu$, the amount and distribution of training data points per normalised load case are part of the optimisation process. For testing and validation, the yield stresses were iteratively defined by finding the root of the decision function of the SVC using the bisection method.

## 3. Elastic properties and anisotropy

The two RVEs described in Section 2.1 were first analysed regarding their elastic material properties. Young's modulus and Poisson's ratio of the RVEs were determined independently for x-, y- and $z$-direction during ideal elastic load-driven simulations with uniaxial load applied at the reference nodes. We find isotropic behaviour in these directions as well as under tensile and compressive loading, which is in accordance with observations from Richert et al. [10] and the RVEs cubic symmetry. The results are listed in Table 2.

Noteworthy is the increased Young's modulus of the Kelvin RVE relative to the diamond RVE. While the ligaments in the diamond RVE are oriented in {111}- directions and, therefore, show mainly bending under uniaxial normal loads [12], the ligaments of the Kelvin RVE are oriented in {110}-directions. Thus, they are partly in-plane to the applied load, which promotes additional axial strains and, therefore, higher stiffness. The shear modulus was determined using pure shearing with $\sigma_{ij} = \sigma_{ji}$. Isotropic behaviour was observed with respect to shearing in the normal directions, similar to the Young's modulus and Poisson's ratio, see Table 2. The shear modulus of the Kelvin RVE nearly coincides with that of an isotropic material $G_{iso} = 2007$ MPa, defined by Eq. (6). In contrast, the diamond RVE yielded a shear modulus

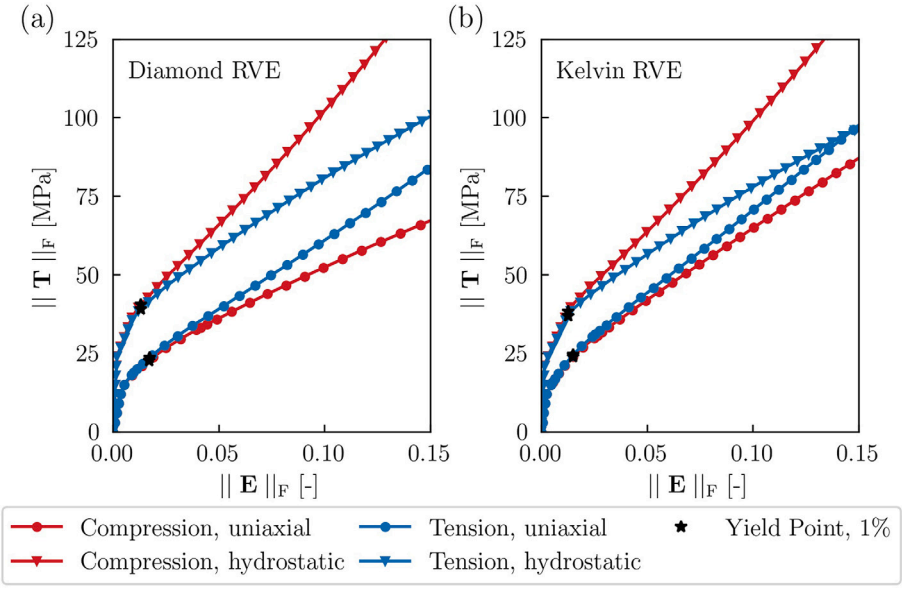


**Fig. 5.** True stress–strain curves for the (a) diamond and (b) Kelvin RVE under uniaxial and hydrostatic tension and compression. Yield stresses at 1% plastic strain are indicated.

**Table 2**
Elastic material properties of the diamond and Kelvin RVE. Young's modulus and Poisson's ratio determined from uniaxial tension/compression and shear moduli from pure shearing are identical in all normal directions. Anisotropy is defined by Eq. (5) as the quotient of the material's computed shear modulus for cubic symmetry and the isotropic shear modulus.

| | Diamond RVE | Kelvin RVE |
|---|---|---|
| Young's modulus [MPa] | 3626.99 | 5217.43 |
| Poisson's ratio [–] | 0.36 | 0.309 |
| Shear modulus [MPa] | 2812.24 | 2017.74 |
| Anisotropy [–] | 2.11 | 1.01 |

**Table 3**
Yield stresses of the considered RVEs under uniaxial ($\sigma_{uni}$) and hydrostatic ($\sigma_{hyd}$) tensile and compressive loading as well as under pure shearing ($\sigma_{shear}$) determined at 1 and 10% plastic strain.

| | Diamond RVE | | | | Kelvin RVE | | | |
|---|---|---|---|---|---|---|---|---|
| | Tension | | Compression | | Tension | | Compression | |
| | 1% | 10% | 1% | 10% | 1% | 10% | 1% | 10% |
| $\sigma_{uni}$ [MPa] | 23.54 | 70.85 | 22.71 | 57.81 | 24.45 | 79.39 | 23.83 | 71.49 |
| $\sigma_{hyd}$ [MPa] | 39.08 | 83.52 | 40.45 | 108.98 | 36.89 | 80.23 | 38.34 | 104.59 |
| $\sigma_{shear}$ [MPa] | 27.68 | 76.08 | – | – | 21.53 | 57.92 | – | – |

considerably larger than the isotropic one of $G_{iso} = 1333.45$ MPa, which leads to a high anisotropy of $A = 2.11$, Eq. (5). The higher stiffness of the diamond RVE under shear deformation is caused by the axial stretching of the ligaments, which are oriented in {111}-directions. While, for the Kelvin RVE, bending still dominates the deformations of the ligaments under shearing. The elastic material properties indicate a cubic anisotropy of the compliance tensor. Thus, perfect predictions of the elastic deformation behaviour, i.e. strain tensors from predefined stress tensors, were possible using Hooke's law of linear elasticity, Eq. (4).

In addition, the compliance tensors were used to define the direction dependent Young's moduli, which are shown in Fig. 1(c) and (d) and clearly display the extent of anisotropy especially for the diamond RVE. The highest stiffness of 6887.28 MPa was found for the diamond RVE for {111}-directions, which exactly corresponds to the ligament orientations in the diamond RVE. These results are in accordance with the cubic symmetry of the structures and preceding studies concerning the diamond or Kelvin structure in varying contexts [19,58].

## 4. Data acquisition: Yield stresses under multiaxial shear and normal load

The prediction of yield stresses using ML techniques requires the generation of training, testing and validation data sets. Data was acquired by determining the onset of plastic yielding at 1% and after hardening at 10% plastic strain in true stress–strain curves from FE simulations with arbitrary multiaxial loads. In the following, yield stresses are first discussed for normal stresses (3D, reduced parameter space) and second for general load cases, considering all 6 independent components of the stress tensor (6D).

### 4.1. Uniaxial and hydrostatic tension/compression

First, the RVEs were deformed independently under uniaxial and hydrostatic tension and compression. The corresponding stress–strain curves are shown in Fig. 5(a) and (b) and the resulting yield stresses in Table 3. These results give first impressions on the magnitude of yield stresses as well as the deformation mechanisms under different loading conditions. In contrast to the Young's modulus under uniaxial loading, which was considerably higher for the Kelvin RVE, both structures showed similar yield stresses under uniaxial loads.

At 1% plastic strain, a slight tension-compression asymmetry was found with 3–4% higher yield stresses under tension compared to compression. The tension-compression asymmetry is a result of different deformation mechanisms and was also observed in earlier studies on similar models [10,12] but also on more random structures in molecular dynamic simulations [65]. Pronounced s-shape bending leads to lower yield stress under compression [12]. Under tension, bending was also observed here but is usually accompanied by reorientation of the ligaments in loading direction followed by stretching and thinning [66].

The deformation behaviour under tension and compression changes when hydrostatic stresses are applied. First, note that unlike common bulk materials, e.g. metals, we find a finite yield stress under hydrostatic loading for open-cell foams. The yield stresses under hydrostatic loading are considerably higher than under uniaxial loading e.g. nearly by a factor of 2 for the diamond RVE under compressive loading, see Table 3 and Fig. 5(a). This is caused by axial compression/stretching of the ligaments, which leads to an increase/decrease of the ligament radius and, thus, of the yield stress. Furthermore, in contrast to the uniaxial loading conditions, the yield stresses under compression exceed those under tension by 3.5 and 3.9% for the diamond and the

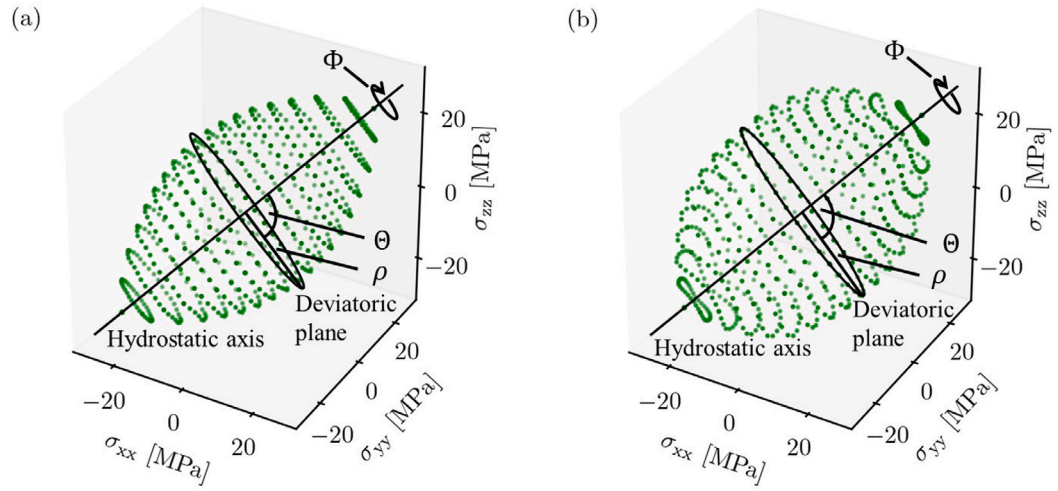


**Fig. 6.** Yield surfaces for the (a) diamond and (b) Kelvin RVE at 1% plastic strain. The angles $\Phi$ and $\Theta$ for the scan of the yield surface, the hydrostatic axis, deviatoric plane and radial component $\rho$ are indicated.

Kelvin RVE, respectively. As true stresses and strains were considered, changes in the cross-sectional area of the RVEs intensified the tension-compression anisotropy at larger strains.

### 4.2. Multiaxial normal loads (3D)

The outcome of the previous section demonstrates that the yield stress is significantly affected by the loading conditions. As a next step, different 3D load conditions were applied to both RVEs in a load controlled simulation and the yield stresses were determined at 1 and 10% plastic strain, see Section 2.2. The yield surface was scanned around the hydrostatic axis. $\Phi$, indicated in Fig. 6(a) and (b), was varied from 0 to 360° in intervals of 10°. The portion of hydrostatic load is represented by the angle $\Theta$ relative to the hydrostatic axis, which was varied from 0 to 180° in steps of 10°, with $\Theta = 0°$ and $\Theta = 180°$ corresponding to points lying on the hydrostatic axis and $\Theta = 90°$ to points in the deviatoric plane. The resulting yield surfaces are shown in Fig. 6(a) and (b) for both RVEs. The yield surfaces narrow from the deviatoric plane to the poles, with maximum yield stresses under hydrostatic loading.

Interesting is the higher anisotropy in form of a 3-fold rotational symmetry around the hydrostatic axis in some regions of the Kelvin RVE, while the diamond RVE shows a nearly circular symmetry. This observation is in contrast to the elastic behaviour, where the Kelvin RVE was nearly isotropic. It must be noted, however, that the directional dependent Young's modulus was calculated for uniaxial loading in different directions and not for multiaxial loading. For $\Theta = \text{const.}$, maxima and minima occur under dominating equibiaxial and uniaxial loading, respectively, due to the ligaments oriented in {110}-directions. The diamond RVE does not have ligaments along these directions and, therefore, does not show preferred directions for $\Theta = \text{const.}$ For 10% plastic strain, additional anisotropic effects occur, which mainly result from using true stresses and strains and, hence, the change in cross-sectional area. For the Kelvin RVE, this effect reduces the observed anisotropy, especially under tension. Hardening mechanisms and the change in ligament orientation during deformation may also cause the observed behaviour.

### 4.3. Combined normal and shear loads (6D)

For further analysis of the mechanical behaviour of the RVEs, shear stresses were applied as pure shearing, multiaxial shearing and in combination with normal stresses (6D stress space). Similar to the previous section, the loads were applied at reference nodes. As can be seen from Table 3, under pure shearing, the diamond RVE shows a 18% higher yield stress than under uniaxial compressive loading, while the yield stress under shear load is 10% lower than under uniaxial compressive loading for the Kelvin RVE. The difference in yield stress of the two RVEs under shearing results from differing deformation mechanisms, which are due to the ligament orientations. The ligaments of the diamond RVE are stretched axially, while the ligaments of the Kelvin RVE show s- and u-shape bending as the major deformation mechanism and thus lead to a lower yield stresses under shearing.

In a next step, multiple shear components were combined. Fifty randomly chosen loading conditions, see Section 2.3, in the space of independent shear stresses were applied to each RVE. The resulting yield surface is nearly spherical such that one representative shear component seems to be sufficient. However, if combined shear and normal stresses are considered, yield stresses depend on the exact combination of stress components such that normal and shear components are not independent of each other. This may be caused by the deformations, which result in changes in cross-sectional area and, for shear stresses, also changes in its orientation. Thus, the three shear components cannot be replaced by one representative component without implementing unknown errors, if additional normal stresses are applied. Therefore, all six independent stress components of the initial stress tensors are considered in this work to prevent potential errors caused by using invariants of the stress tensor.

For 6D load cases, a dataset was prepared with 800 randomly selected load cases with six independent stress components (see Section 2.3). Uniqueness of each load case in the dataset was ensured. The resulting components of the tensor were applied as loads to both RVEs in the simulations. The yield stresses were determined from the simulation data of the elastic–plastic FE simulations at 1 and 10% plastic strain, resulting in 3200 data sets in total. The yield surfaces turned out to be highly anisotropic, as will be shown in context of the discussion of the Deshpande-Fleck model in Section 5.1. A random selection of these stress vectors and yield stresses are used as training and validation data in the course of this work. For testing, an additional dataset of 200 load cases per RVE was created in the same manner.

## 5. Predicting yield stresses

In case of general multiaxial loading, obtaining yield stresses from simulation data is computationally demanding. Therefore, we seek for possibilities to predict yield surfaces in an effective manner. First, the potential and limits of the Deshpande-Fleck model for isotropic solid foams for the prediction of the here considered yield surfaces are

**Table 4**
Parameters used for fitting the Deshpande-Fleck model to the simulation data. The ellipticity parameter $\alpha$ was determined from the yield stress under uniaxial ($\sigma_{uni}$) loading and the mean hydrostatic yield stress ($\sigma_{hyd,m}$) at 1 and 10% plastic strain.

| | Diamond RVE | | Kelvin RVE | |
|---|---|---|---|---|
| | 1% | 10% | 1% | 10% |
| $\sigma_{uni}$ [MPa] | 22.71 | 57.81 | 23.83 | 71.49 |
| $\sigma_{hyd,m}$ [MPa] | 23.35 | 62.92 | 22.14 | 60.39 |
| $\alpha$ [–] | 1.028 | 0.965 | 1.153 | 1.289 |

analysed. In the second part, the analysed simulation data, i.e. the yield stresses as a function of loading direction, are used to train and optimise the machine learning algorithms introduced in Section 2.4. Their ability to predict yield stresses with regard to the necessary amount of training data and their generalisability are evaluated.

### 5.1. Deshpande-Fleck model

The first approach for the prediction of yield stresses is the Deshpande-Fleck model for isotropic solid foams [33]. To fit this model to our data, the parameter $\alpha$ was determined from $\sigma_{uni}$ and $\sigma_{hyd,m}$ under compression, analysed in Section 4.1, using Eq. (14). Values of $\sigma_{uni}$, $\sigma_{hyd,m}$ and $\alpha$ for the considered RVEs and for 1 and 10% plastic strain are listed in Table 4. To compare the yield stresses determined in Section 4 to the Deshpande-Fleck yield function in $\sigma_m - \sigma_e$-space, they had to be transferred to $\sigma_{e,S}$ and $\sigma_{m,S}$, as described in Section 2.2.1. $\sigma_{e,S}$ and $\sigma_{m,S}$ and the points of the Deshpande-Fleck yield function were scaled with the yield stress at uniaxial compression and plotted for both RVEs and 3D load cases in Fig. 7(a) and (b).

The Deshpande-Fleck yield function is a good first estimation for the prediction of the yield stresses for the diamond RVE and for small strains, with relative errors smaller than 10%. For the Kelvin RVE and also for larger strains, maximum errors of up to 30% occur. The pronounced scattering of the points is a result of the anisotropy of the yield surface, especially regarding the 3-fold rotational symmetry, found in Section 4.2. The scattering occurs for constant angle $\Theta$ relative to the hydrostatic axis, defined in Fig. 6, and thus constant angle $\gamma$ and triaxiality, defined in Fig. 4. For the Kelvin RVE, all points around $\sigma_m = 0$ are not in proximity to the Deshpande-Fleck yield function. This is due to the high strength under dominating (equi-)biaxial loads, caused by the ligament orientations in {110}-directions. In addition, as expected, the isotropic Deshpande-Fleck model does not capture the tension-compression asymmetry. The large deviations raise the question, if the parameter $\alpha$, determined from $\sigma_{uni}$ and $\sigma_{hyd,m}$, leads to an optimal fit of the Deshpande-Fleck model to our data. Applying the least-squares method on the whole data set to find $\alpha$ for the Kelvin cell and 3D load cases results in a perfect agreement with $\alpha$ determined from Eq. (14), see Fig. 7(b). Thus, Eq. (14) already gives the best fit for the Deshpande-Fleck yield criterion.

Even more scattering was observed for loading conditions, which include shear and normal stresses, see Fig. 7(c) and (d). In this case, in contrast to multiaxial normal stresses, the diamond RVE shows the largest deviations. This is due to the anisotropy with regard to normal and shear loading, i.e. the higher yield stresses under shearing compared to uniaxial loading, see Table 3. These deviations are even larger than for normal stresses for both 1 and 10% plastic strain. Thus, the yield surfaces can barely be described by the Deshpande-Fleck yield function. For the diamond RVE, the Deshpande-Fleck yield function mainly underestimates the yield stresses from simulation. For the Kelvin RVE, yield stresses are underestimated especially for small strains, while they are overestimated at large strains for high $|\sigma_m|$.

A least-squares fit of the Deshpande-Fleck model to the 6D data of the diamond and Kelvin RVE at 1% plastic strain results in $\alpha = 1.328$ and 1.447, respectively. As such, considerably greater values than predicted using Eq. (14), see Table 4, are found, which indicates that $\alpha$ might require an extended definition for complex load cases including normal and shear loads, which is not in the scope of this work, as these parameters do not lead to major improvements, see Fig. 7(c) and (d). Relying on this and in order to use as few data and parameters as possible for the underlying physical model, we decided to further use the parameter $\alpha$ defined by Eq. (14), even though it may not lead to an optimal fit. Furthermore, convergence limitations occurred during the least-square fit of the yield surfaces of the diamond RVE at large plastic strains, Fig. 7(a).

In Fig. 7(c) and (d), note that nearly no points are present for $\sigma_e < 0.4$, compared to normal loads as shown in Fig. 7(a) and (b). This implies that stress tensors with high hydrostatic portion but without further shear loads might be underrepresented in the training data. This is seen as an opportunity to validate the ability of generalisation and extrapolation of the trained ML approaches, which will be discussed in Section 5.2.

### 5.2. Machine learning techniques

As the Deshpande-Fleck yield function does not give a satisfactory description of the observed yield surfaces of the RVEs, ML algorithms are used to predict the yield surface in 3D and 6D stress space. We use a data-driven ANN, a hybrid ANN, which corrects the yield stresses from the Deshpande-Fleck model, and SVC. In the following, we describe the preprocessing of the data sets as well as the procedure to find the optimal hyperparameters and amount of training data for these approaches. Lastly, we will test the trained approaches with regard to their accuracy and ability for generalisation and extrapolation.

#### 5.2.1. Preparation of input data and models

The yield surfaces that were compared to the Deshpande-Fleck model for isotropic solid foams in Section 5.1 are used as training and validation data. First the validation data is selected randomly from these data sets, followed by a random choice of training sets from the remaining data sets. For testing of the optimised model, separate data sets are prepared. The data must be provided in a manner that the algorithms are able to map and predict the relationship between yield stress/output parameter and the input features, i.e. stress vector normalised to unit length, as given in Eq. (19), plastic strain (1 and 10%) and structure (0: Kelvin, 1: Diamond). Normalisation of the stress vector is important, because it makes sure that (i) only the contribution of the components to the stress tensor/vector have to be evaluated instead of additional evaluation of the norm's influence and (ii) the input data is dimensionless, due to scaling with the Frobenius norm. These factors improve the training process and, as such, also the performance of the trained ML model. For SVC, several points above and below the yield stress are necessary to define one point on the yield surface, resulting in larger amounts of training data.

The yield stress is the desired target parameter for all approaches. The procedure for its prediction and the output variables in the different methods were discussed in more detail in Sections 2.4.1–2.4.3. In addition to the normalisation of the stresses, the input features and output variables were standardised by adding the StandardScaler, provided by the scikit-learn package [62,63], to a pipeline.

#### 5.2.2. Optimisation and training

First, the hyperparameters of the ML algorithms were optimised. Therefore, the amount of training data was chosen such that a good compromise between minimum error and computational cost i.e. number of simulations is achieved. The amount of load cases used during the optimisation process for training and validation for both load cases are given in Table 5. For ANNs, the hyperparameters described in Section 2.4.1 were optimised using the RandomisedSearchCV algorithm, provided by the scikit-learn package [62,63]. To keep computational time low and prevent overfitting, due to the relatively small amount

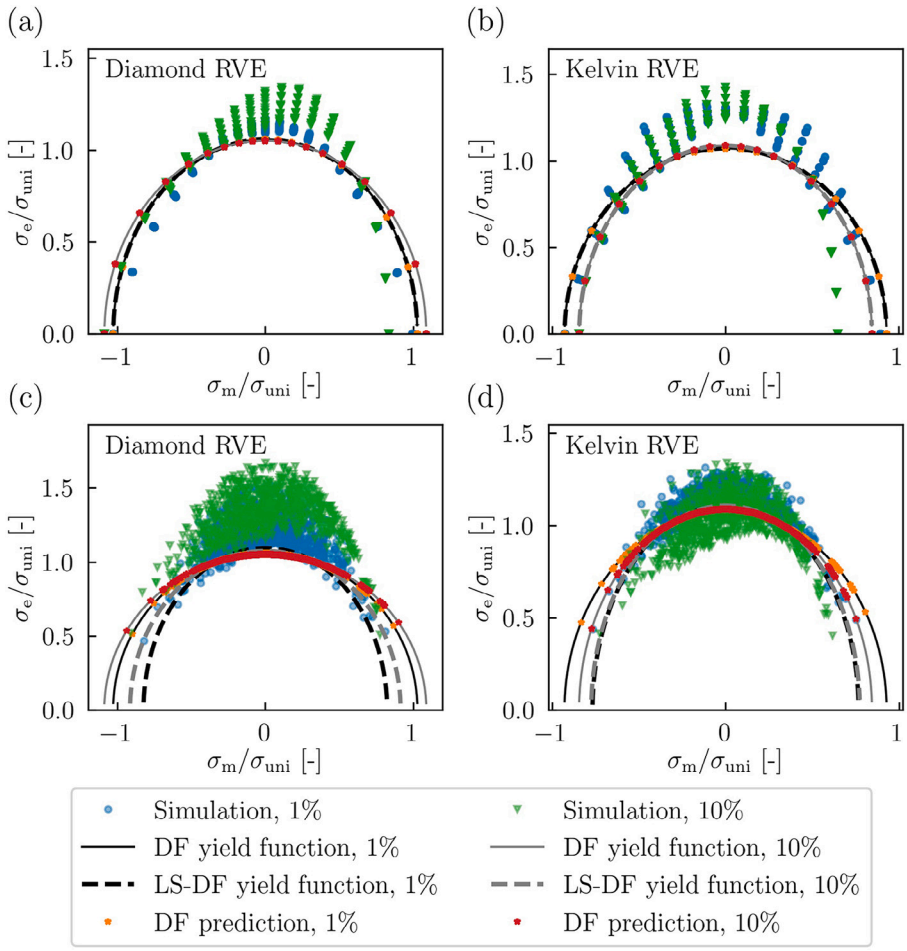


**Fig. 7.** Yield stresses from FE simulations at 1 and 10% plastic strain for the (a) diamond and (b) Kelvin RVE for 3D load cases, as well as for the (c) diamond and (d) Kelvin RVE for 6D load cases. Yield stresses are plotted along with the results from the Deshpande-Fleck ('DF') model for isotropic solid foams in space of mean hydrostatic ($\sigma_m$) and effective stress ($\sigma_e$), normalised with the uniaxial yield stress ($\sigma_{uni}$). The fitting parameter $\alpha$ was determined from Eq. (14) ('DF') as well as a least-square fit of all data points ('LS-DF'). For (a) the least square fit did not converge at 10% plastic strain.

**Table 5**
Number of training and validation data for optimisation of the hyperparameters and learning curves.

| | Optimisation | | Learning curves | |
|---|---|---|---|---|
| | Training | Validation | Training | Validation |
| 3D | 400 | 300 | 50–900 | 300 |
| 6D | 900 | 300 | 50–1500 | 300 |

**Table 6**
Parameters found during the optimisation process of the data-driven and hybrid ANN for training with 3D and 6D load cases. $\lambda$ is the regularisation parameter. The number of neurons are given as neurons per hidden layer i.e. (1st layer, 2nd layer...). As solver, the L-BFGS algorithm is used in all cases.

| Load cases | Data-driven ANN | | Hybrid ANN | |
|---|---|---|---|---|
| | 3D | 6D | 3D | 6D |
| Activation function | tanh | tanh | ReLU | tanh |
| $\lambda$ [–] | $1.0\times10^{-6}$ | $1.0\times10^{-4}$ | $1.0\times10^{-2}$ | $1.0\times10^{-2}$ |
| Neurons | (20,20) | (30) | (30,30) | (30,10) |

of processed data, a maximum of 2 hidden layers, with a few tens of neurons each, were considered. In our case, the optimal solver for weight optimisation is L-BFGS. The remaining hyperparameters depend on the amount of stress components, i.e. 3D or 6D load cases, and the chosen approach, i.e. data-driven or hybrid approach. The optimised parameters are listed in Table 6.

**Table 7**
Parameters found during the optimisation process of the SVC with RBF kernel for training with 3D and 6D load cases. C is the L2 regularisation parameter and $\mu$ controls the influence of a single training set. The factor of 0.05 for standard deviation represents a good compromise between accuracy and computation time.

| Parameters SVC | |
|---|---|
| $C$ | 1000 |
| $\mu$ | 0.1 |
| Points/load case for training | 50 |
| Standard deviation | $0.05\sigma_Y$ |

For SVC, the parameters mentioned in Section 2.4.3 were optimised. The common RBF kernel was chosen similar to [54]. The points per load case in the training data sets were drawn from a normal distribution around the yield stress. The number of points and the standard deviation of this distribution was optimised. The resulting optimised parameters were found to be similar for the training with 3D and 6D load cases and are listed in Table 7.

Learning curves for the approaches with optimised parameters are shown in Fig. 8(a) and (b) for 3D and 6D load cases, respectively. The mean relative approximation error

$$\overline{\delta_Y} = \frac{1}{N}\sum_{i=1}^{N}\frac{|\sigma_{Y,ML} - \sigma_{Y,S}|}{\sigma_{Y,S}} \tag{25}$$

of the yield stresses predicted for $N$ validation data points, s. Table 5, is plotted vs. the number of yield points used for training to visualise the

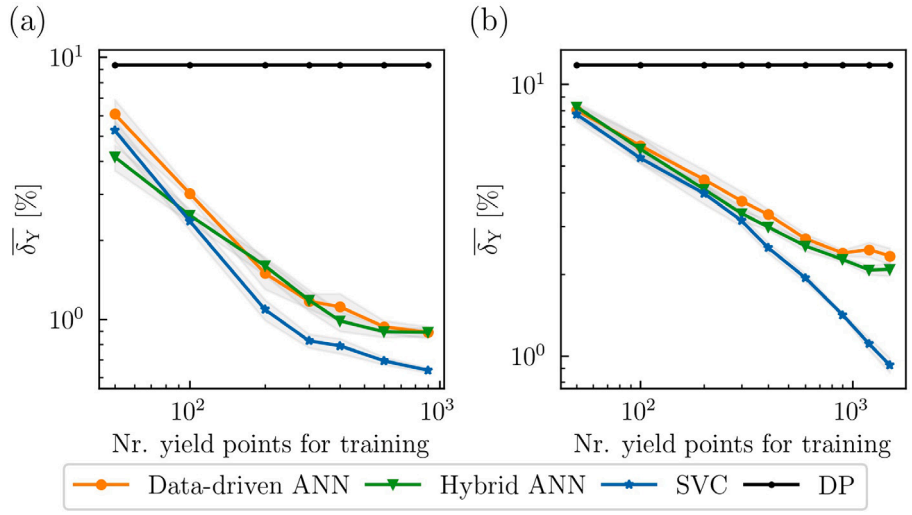


**Fig. 8.** Learning curves showing the mean relative approximation error $\overline{\delta_Y}$ for non-training samples vs. number of yield points used for training of the considered approaches for (a) 3D and (b) 6D load cases. In addition, the mean relative approximation error of the mere Deshpande-Fleck model (DP) is given.

convergence behaviour. $\sigma_{Y,ML}$ and $\sigma_{Y,S}$ are yield stresses determined from ML approaches and FE simulations, respectively. The validation sets are kept identical for every point in the learning curve. For 3D load cases, Fig. 8(a), the error decreases linearly for small amounts of yield points used for training. The hybrid approach, introduced in Section 2.4.2, yields smallest errors when very few training data sets are provided. This is in agreement with our expectations and previous studies on hybrid modelling approaches [41,42,67]. Convergence of the relative approximation error to approximately 1% starts at 300 and 400 data sets for the data-driven and hybrid ANN, respectively. Slightly better results are achieved for SVC, when trained with more than 200 load cases and convergence sets in above 300 data sets.

In case of 6D load cases, shown in Fig. 8(b), the errors, which are nearly identical for all approaches, decrease linearly below 400 training data sets. In the considered range of training data, convergence is not as obvious as for 3D load cases. However, when more than 600 yield points are used for training, the slope decreases (less negative) for the ANNs, leading to an increasing better performance of the SVC, which already exceeds the results of the hybrid and data-driven ANN by up to 0.9% for 900 load cases. These are surprising results, as the hybrid model was expected to lead smaller errors compared to the purely data-driven approaches, especially for small amounts of training data and an extended parameter space [67].

Mean relative errors as small as for 3D load cases could not be reached and no convergence was observed for the SVC within the available amount of simulation data in Fig. 8(b). This may be due to the pronounced anisotropy of the yield surfaces especially with regard to the Kelvin RVE. In addition, it was expected that by increasing the feature space from 3 to 6 stress components, considerably more data is necessary to represent the yield surface [55]. However, for our application, errors of only 1–3% for validation are considered sufficient. Therefore, the additional computational effort necessary to decrease the error by using more load cases for training is not considered reasonable.

#### 5.2.3. Testing of the optimised models for reduced parameter space (3D)

For testing of the approaches trained with 3D load cases, data from 100 simulations with randomly chosen stress vectors were used for each structure. As the yield stresses at 1 and 10% plastic strain were considered, 400 data sets were available for the testing, see Table 8. Training was performed using 400 3D load cases chosen randomly from the yield surfaces discussed in Section 4.2. For SVC, this corresponds to $400 \times 50 = 20000$ data sets for training. Compared to the mean error of 8% achieved with the Deshpande-Fleck model, the predictions of the yield stresses during testing lead to remarkably small mean relative errors, see Table 8. Best results are achieved using SVC, while the hybrid model does not yield considerably better results than both data-driven approaches. All approaches show a clear improvement to the Deshpande-Fleck yield function with the drawback that considerably more data is required.

**Table 8**
Number of load cases used for training and testing of the approaches. The total number of training data points for SVC is achieved by multiplying the given number with the amount of points per load case (50). The resulting error during testing is given for all approaches. The 3D yield surfaces, Section 4.2, are used for testing in the last two rows.

| Training | | Testing | | Error [%] | | |
|---|---|---|---|---|---|---|
| 3D | 6D | 3D | 6D | ANN | Hybrid | SVC |
| 300 | – | 400 | – | 1.2 | 1.1 | 0.8 |
| – | 600 | – | 800 | 2.7 | 2.4 | 1.9 |
| – | 600 | 2456 | – | 4.4 | 3.9 | 2.5 |
| 100 | 500 | 2456 | – | 3.1 | 2.7 | 1.7 |

#### 5.2.4. Testing of the optimised models for general parameter space (6D)

For 6D load cases, training was carried out using 600 randomly chosen points on the 6D yield surfaces, even though better results could be achieved with more training data for SVC. This reduces the computational effort and using the same amount of yield points for training of all approaches allows for better comparability. For SVC, $600 \times 50 = 30000$ training data sets were used in total. The number of load cases used for training and testing, as well as the resulting errors are summarised in Table 8. First, testing was performed using 800 data sets with 6D load cases: 200 for each structure and each plastic strain. As expected from the learning curve in Fig. 8(b), SVC shows the smallest error of 1.9%. Furthermore, the hybrid model outperformed the data-driven ANN only marginally by 0.3%, see Table 8.

In Section 5.1, we discussed that pure (hydrostatic) normal loads are underrepresented in the randomly distributed 6D load cases used for training. This allows for testing the ability of the approaches to extrapolate, i.e. predict yield stresses outside the range of training data. To this end, the yield stresses for 3D load cases from Fig. 6 were taken as a second testing set, resulting in 2456 data points. For the hybrid model, we expected better accuracy and efficiency compared to the data-driven approaches for points entirely outside the range of training data. The underlying physics in form of the Deshpande-Fleck model should yield a first approximation, see Section 5.1, and, therefore, prevent large discrepancies. The 45° scatter plots in Fig. 9(a)–(c) show the yield stresses acquired from the ML approaches vs. those

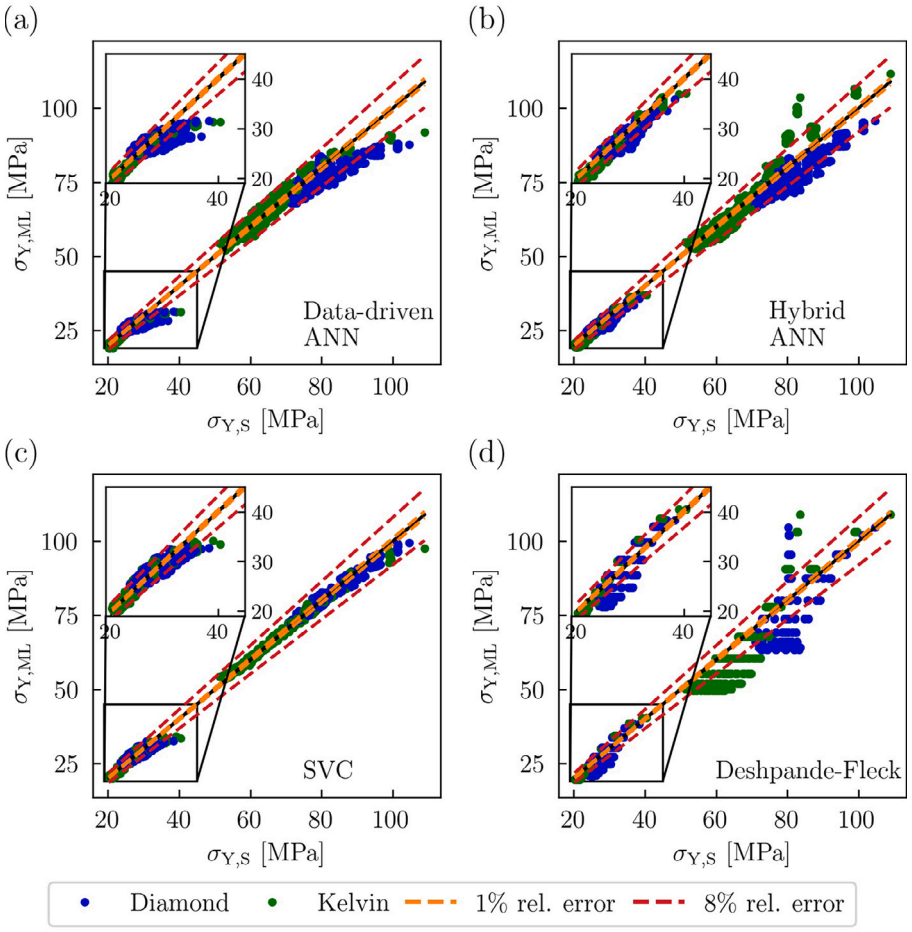


**Fig. 9.** 45° scatter plot for testing with 3D load cases of the ML models trained with 6D load cases. Yield stresses of the diamond (triangles) and Kelvin (points) RVE predicted with the (a) data-driven ANN, (b) hybrid ANN, (c) SVC and (d) only the Deshpande-Fleck model ($\sigma_{Y,ML}$) are compared to the results from simulation data ($\sigma_{Y,S}$). Yield stresses in the range 20 to approximately 40 MPa were determined for 1% and those above at 10% plastic strain. Dashed lines indicate error limits of 1 and 8%, the latter corresponding to the mean relative error of the Deshpande-Fleck model for 3D load cases.

from FE simulations for the testing with 3D load cases. In addition, Fig. 9(d) shows the yield stresses predicted with the pure Deshpande-Fleck model. The mean relative approximation errors are given in Table 8.

The results of the ANN approaches in Fig. 9(a) and (b) reveal that larger yield stresses for both 1 and 10% plastic strain, which are those with high amount of hydrostatic loading, are predicted with major deviations. For the data-driven approach, Fig. 9(a), the yield stresses outside of the training range are underestimated and only slightly scattered around nearly constant yield stresses ($\sigma_{Y,ML}$) of 30 and 80 MPa for 1 and 10% plastic strain, respectively. For the hybrid model, Fig. 9(b), the predictions at 1% plastic strain agree well with the yield stresses from FE simulation data. In contrast, the scattering was more pronounced for yield stresses determined at 10% plastic strain, especially for the diamond RVE. The yield stresses of the diamond RVE are mostly overestimated, while those of the Kelvin cell are underestimated.

The predicted yield stresses of the diamond RVE in Fig. 9(b) show obvious similarities with the predictions of the lone Deshpande-Fleck model in Fig. 9(d). However, the scattering is more pronounced along the $\sigma_{Y,ML}$-axis in the hybrid model, caused by different corrections for certain load cases, which are represented by a single point in the Deshpande-Fleck model, see Fig. 7(c) and (d). For the Kelvin RVE, the better balance regarding the ratio of points below and above the Deshpande-Fleck yield function, see Fig. 7(d), may result in the more accurate, less biased prediction of the corrections.

These observations clearly show that the gain in efficiency is highly dependent on the ability of the underlying model to represent the data. Pronounced scattering around the Deshpande-Fleck yield function limits the ability of the ANN to find a sufficiently accurate relationship between the input features and the corrections, which is the general idea behind a hybrid approach. Therefore, the here proposed hybrid model is in effect comparable to a data-driven ANN and, therefore, does not lead to a better efficiency.

The limitations for extrapolation can be overcome by adding 3D load cases to the training data [55]. Fig. 10 and the test results in Table 8 clearly show the improvement for the prediction of yield stresses in 3D stress space, when a fraction of the training data is replaced by 3D load cases. Apparently, this leads to decreased accuracy for the prediction of yield stresses under 6D loading. An optimum is reached when 100 of the total 600 6D load cases for training are substituted by 3D load cases, as it leads to a significant improvement for testing with 3D load cases, while the decrease for testing with 6D load cases is negligible

While the approaches using ANNs, trained with only 6D load cases, have difficulties predicting yield stresses outside the range of training data, SVC yields convincing results with a mean relative error of 2.5% and, therefore, an astonishingly good ability for generalisation and extrapolation. Besides, Fig. 9(c) shows that only a few points exceeded the mean relative error of the Deshpande-Fleck model of 8%, indicated by dashed lines.

On the example of the SVC, we found that different randomly chosen data sets for training with the same size can lead to relatively small variations in mean approximation error between 2.4 and 3.2% for

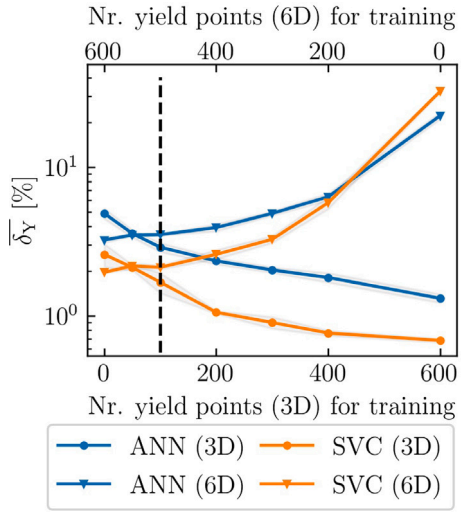


**Fig. 10.** Dependency of the mean approximation error $\delta_Y$ from the amount of points from 3D and 6D yield surfaces used for the training of artificial neural networks (ANN) and support vector classification (SVC), while keeping total number training data points constant at 600. Validation was performed using sets of only 3D (circles) or only 6D (triangles) load cases.

5 iterations. This shows that the selection of training data can be crucial but in our case does not lead to major improvements and does not affect the better suitability of the SVC compared to the ANNs. However, similar to the ANNs, the SVC can be further improved by training with 100 3D and 500 6D load cases, resulting in a mean relative error of 1.7%.

The cause of the high generalisability of the SVC algorithm compared to the ANNs is most likely caused by the nature of the hyperplane definition combined with a convex optimisation algorithm. Based on this, for ANNs, better results might be achieved by using architectures, which ensure convexity between the inputs and outputs [47]. Using a classification instead of a regression algorithm could be another reason for the different behaviour of SVCs. Further investigation towards the use of ANN as a classifier or a support vector regressor might give a deeper inside, but were not part of this work.

The resulting yield surfaces for biaxial load cases in the $\sigma_{xx} - \sigma_{yy}$-and $\sigma_{zz} - \sigma_{xy}$-plane, predicted with the Deshpande-Fleck model and the SVC, trained with combined 3D and 6D load cases, are shown in Fig. 11(a),(c) and (b),(d) for the diamond and Kelvin RVE, respectively. Larger deviations to the yield stresses from simulation data are observed for predictions with the Deshpande-Fleck model in contrast to the relatively small deviations of the SVC, especially with regard to yield stresses under shearing, see Fig. 11(c) and (d). This is in agreement with the observations of the deviating fitting parameter $\alpha$ found with the least-square method in Section 5.1. Furthermore, deviations occur in the $\sigma_{xx} - \sigma_{yy}$-plane when yield stresses are predicted for biaxial loading with components of opposite sign.

The full 3D yield surface at 1% plastic strain predicted by the trained SVC and the Deshpande-Fleck model is shown together with the simulation data in Fig. 12(a) and (b) for the diamond and Kelvin RVE, respectively. The results indicate that the SVC yields very good predictions for the cylindrical symmetry of the diamond RVE, which are limited for high amounts of hydrostatic loads, which is in agreement with the observations in Fig. 9(c), when the SVC was trained with only 6D load cases. For the Kelvin RVE, further limitations occur for the prediction of the rotational anisotropy around the hydrostatic axis. These limitations could be caused by the small amount of 3D load cases for training and could, thus, be improved by using more training data. However the results of the SVC still show major improvements to the Deshpande-Fleck model.

## 6. Conclusions

We investigated the elastic–plastic mechanical response of RVEs with idealised diamond and Kelvin structure under multiaxial loads using FE simulations. At small strains, the material behaviour follows Hooke's law of linear elasticity with cubic anisotropy. The onset of plastic yielding was analysed for 1 and 10% plastic strain. In both cases we observed a varying extent of anisotropy for the yield surfaces of the two RVEs, which could not be described using existing models such as the Deshpande-Fleck model for isotropic solid foams.

Three ML algorithms were studied with regard to their potential to describe yield surfaces in 3D and 6D stress space for different types of structure as well as included hardening behaviour under radial loading. We showed that SVC gives best results and allows for good generalisation and extrapolation, probably due to its convex nature. Therefore, it allows a promising description of the 6D yield surface for complex compressive materials with pronounced anisotropy. Compared to the SVC, the approaches using ANNs were unable to predict load cases outside the training range and converged at larger errors. For the data-driven ANN, the cause may be the missing convexity, which might be improved by using (partially) input convex neural networks. Against our expectations, the hybrid model, which corrects the Deshpande-Fleck model using ANNs, does not show higher efficiency, e.g. same error for smaller amounts of training data, for general 6D load cases compared to the data-driven algorithms. This shows that the efficiency of a hybrid model is not always beneficial and depends on the overall predictive capability of the underlying model. Because the Deshpande-Fleck model deviates considerably for load cases that include shear components, the ability of the ANN to learn the corrections is limited and, thus, the performance of the hybrid model is comparable to a purely data-driven ANN.

## CRediT authorship contribution statement

**Lena Dyckhoff:** Conceptualisation, Methodology, Software, Investigation, Formal analysis, Writing – original draft, Visualisation. **Norbert Huber:** Conceptualisation, Methodology, Software, Writing – review & editing, Supervision.

## Declaration of competing interest

The authors declare that they have no known competing financial interests or personal relationships that could have appeared to influence the work reported in this paper.

## Data availability

Data will be made available on request.

## Acknowledgements

Lena Dyckhoff and Norbert Huber kindly acknowledge Markus Schuhmacher for the implementation of the finite element beam model with Kelvin architecture.

## Funding

This work was supported by the Deutsche Forschungsgemeinschaft (DFG, German Research Association) [Project Number 192346071 – SFB986].

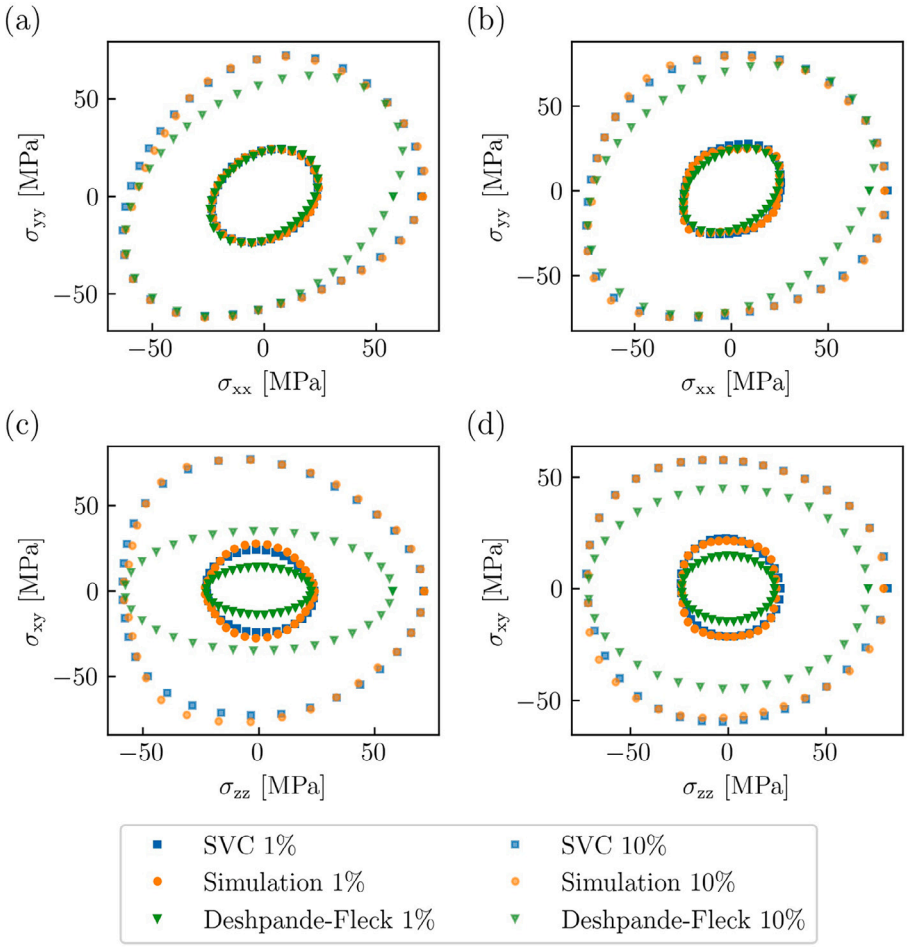


**Fig. 11.** Yield loci for biaxial loading in $\sigma_{xx} - \sigma_{yy}$-plane for (a) diamond and (b) Kelvin RVE as well as in $\sigma_{zz} - \sigma_{xy}$-plane for the (c) diamond and (d) Kelvin RVE determined with the Deshpande-Fleck model, the Support Vector Classification (SVC, trained on 3D+6D load cases) and from simulation data at 1 and 10% plastic strain.

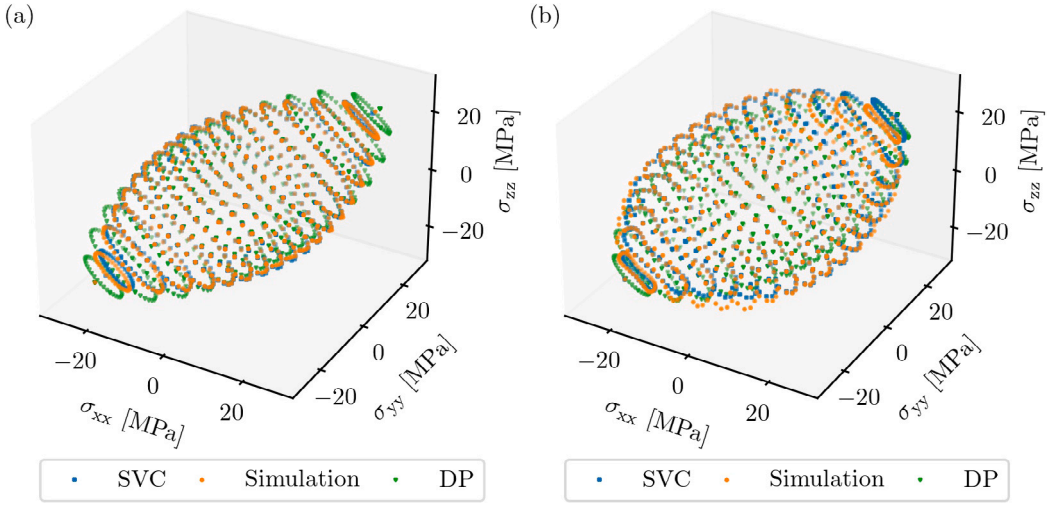


**Fig. 12.** Yield surface of (a) diamond and (b) Kelvin RVE in 3D stress space at 1% plastic strain determined from simulation data, Support Vector Classification (SVC, trained on 3D+6D load cases) and Deshpande-Fleck model(DP).

## References


[1] Wittstock A, Biener J, Bäumer M. Nanoporous gold: a new material for catalytic and sensor applications. Phys Chem Chem Phys 2010;12(40):12919–30. http://dx.doi.org/10.1039/C0CP00757A.

[2] Juarez T, Biener J, Weissmüller J, Hodge AM. Nanoporous metals with structural hierarchy: A review. Adv Energy Mater 2017;19(12):1700389. http://dx.doi.org/10.1002/adem.201700389.

[3] Kim SH. Nanoporous gold: Preparation and applications to catalysis and sensors. Curr Appl Phys 2018;18(7):810–8. http://dx.doi.org/10.1016/j.cap.2018.03.021.

[4] Jin H-J, Weissmüller J, Farkas D. Mechanical response of nanoporous metals: A story of size, surface stress, and severed struts. MRS Bull 2018;43(1):35–42. http://dx.doi.org/10.1557/mrs.2017.302.

[5] Richert C, Huber N. A review of experimentally informed micromechanical modeling of nanoporous metals: From structural descriptors to predictive structure–property relationships. Materials 2020;13(15):3307. http://dx.doi.org/10.3390/ma13153307.

[6] Weissmüller J, Sieradzki K. Dealloyed nanoporous materials with interface-controlled behavior. MRS Bull 2018;43(1):14–9. http://dx.doi.org/10.1557/mrs.2017.299.

[7] Shi S, Li Y, Ngo-Dinh B-N, Markmann J, Weissmüller J. Scaling behavior of stiffness and strength of hierarchical network nanomaterials. Science 2021;371(6533):1026–33. http://dx.doi.org/10.1126/science.abd9391.

[8] Mameka N, Wang K, Markmann J, Lilleodden ET, Weissmüller J. Nanoporous gold—Testing macro-scale samples to probe small-scale mechanical behavior. Mater Res Lett 2016;4(1):27–36. http://dx.doi.org/10.1080/21663831.2015.1094679.

[9] Jiao J, Huber N. Deformation mechanisms in nanoporous metals: Effect of ligament shape and disorder. Comput Mater Sci 2017;127:194–203. http://dx.doi.org/10.1016/j.commatsci.2016.10.035.

[10] Richert C, Odermatt A, Huber N. Computation of thickness and mechanical properties of interconnected structures: accuracy, deviations, and approaches for correction. Front Mater 2019;6:327. http://dx.doi.org/10.3389/fmats.2019.00327.

[11] Li Y, Dinh Ngo B-N, Markmann J, Weissmüller J. Topology evolution during coarsening of nanoscale metal network structures. Phys Rev Mater 2019;3:076001. http://dx.doi.org/10.1103/PhysRevMaterials.3.076001.

[12] Huber N, Viswanath R, Mameka N, Markmann J, Weißümller J. Scaling laws of nanoporous metals under uniaxial compression. Acta Mater 2014;67:252–65. http://dx.doi.org/10.1016/j.actamat.2013.12.003.

[13] Briot NJ, Balk TJ. Developing scaling relations for the yield strength of nanoporous gold. Philos Mag 2015;95(27):2955–73. http://dx.doi.org/10.1080/14786435.2015.1078512.

[14] Griffiths E, Bargmann S, Reddy B. Elastic behaviour at the nanoscale of innovative composites of nanoporous gold and polymer. Extreme Mech Lett 2017;17:16–23. http://dx.doi.org/10.1016/j.eml.2017.09.006.

[15] Davoodi Kermani I, Dyckhoff L, Aydin RC, Huber N, Cyron CJ. Simulated annealing framework for generating representative volume elements of materials with complex ligamentous microstructures. Comput Mater Sci 2023;228:112302. http://dx.doi.org/10.1016/j.commatsci.2023.112302.

[16] Gibson LJ, Ashby MF. Cellular solids: Structure and properties. Cambridge solid state science series, 2nd ed.. Cambridge: Cambridge University Press; 1997, http://dx.doi.org/10.1017/CBO9781139878326.

[17] Gibson IJ, Ashby MF. The mechanics of three-dimensional cellular materials. Proc R Soc Lond Ser A Math Phys Eng Sci 1997;382(1782):43–59. http://dx.doi.org/10.1098/rspa.1982.0088.

[18] Van Der Burg MWD, Shulmeister V, Van Der Geissen E, Marissen R. On the linear elastic properties of regular and random open-cell foam models. J Cell Plast 1997;33(1):31–54. http://dx.doi.org/10.1177/0021955X9703300103.

[19] Luxner MH, Stampfl J, Pettermann HE. Numerical simulations of 3D open cell structures – influence of structural irregularities on elasto-plasticity and deformation localization. Int J Solids Struct 2007;44(9):2990–3003. http://dx.doi.org/10.1016/j.ijsolstr.2006.08.039.

[20] Saane SSR, Mangipudi KR, Loos KU, De Hosson JTM, Onck PR. Multiscale modeling of charge-induced deformation of nanoporous gold structures. J Mech Phys Solids 2014;66:1–15. http://dx.doi.org/10.1016/j.jmps.2014.01.007.

[21] Huber N. Connections between topology and macroscopic mechanical properties of three-dimensional open-pore materials. Front Mater 2018;5. http://dx.doi.org/10.3389/fmats.2018.00069.

[22] Huber N, Ryl I, Wu Y, Hablitzel M, Zandersons B, Richert C, Lilleodden E. Densification of nanoporous metals during nanoindentation: The role of structural and mechanical properties. J Mater Res 2023;38(3):853–66. http://dx.doi.org/10.1557/s43578-022-00870-1.

[23] Gong L, Kyriakides S, Jang WY. Compressive response of open-cell foams. Part I: Morphology and elastic properties. Int J Solids Struct 2005;42(5):1355–79. http://dx.doi.org/10.1016/j.ijsolstr.2004.07.023.

[24] Jang W-Y, Kraynik AM, Kyriakides S. On the microstructure of open-cell foams and its effect on elastic properties. Int J Solids Struct 2008;45(7):1845–75. http://dx.doi.org/10.1016/j.ijsolstr.2007.10.008.

[25] Storm J, Abendroth M, Kuna M. Numerical and analytical solutions for anisotropic yield surfaces of the open-cell Kelvin foam. Int J Mech Sci 2016;105:70–82. http://dx.doi.org/10.1016/j.ijmecsci.2015.10.014.

[26] Roschning B, Huber N. Scaling laws of nanoporous gold under uniaxial compression: Effects of structural disorder on the solid fraction, elastic Poisson's ratio, Young's modulus and yield strength. J Mech Phys Solids 2016;92:55–71. http://dx.doi.org/10.1016/j.jmps.2016.02.018.

[27] Jiao J, Huber N. Effect of nodal mass on macroscopic mechanical properties of nanoporous metals. Int J Mech Sci 2017;134:234–43. http://dx.doi.org/10.1016/j.ijmecsci.2017.10.011.

[28] Richert C, Huber N. Skeletonization, geometrical analysis, and finite element modeling of nanoporous gold based on 3D tomography data. Metals 2018;8(4):282. http://dx.doi.org/10.3390/met8040282.

[29] Odermatt A, Richert C, Huber N. Prediction of elastic-plastic deformation of nanoporous metals by FEM beam modeling: A bottom-up approach from ligaments to real microstructures. Mater Sci Eng A 2020;791:139700. http://dx.doi.org/10.1016/j.msea.2020.139700.

[30] Huber N. A strategy for dimensionality reduction and data analysis applied to microstructure–property relationships of nanoporous metals. Materials 2021;14(8):1822. http://dx.doi.org/10.3390/ma14081822.

[31] Lührs L, Soyarslan C, Markmann J, Bargmann S, Weissmüller J. Elastic and plastic Poisson's ratios of nanoporous gold. Scr Mater 2016;110:65–9. http://dx.doi.org/10.1016/j.scriptamat.2015.08.002.

[32] Mangipudi K, Epler E, Volkert C. On the multiaxial yielding and hardness to yield stress relation of nanoporous gold. Scr Mater 2018;146:150–3. http://dx.doi.org/10.1016/j.scriptamat.2017.11.033.

[33] Deshpande V, Fleck N. Isotropic constitutive models for metallic foams. J Mech Phys Solids 2000;48(6):1253–83. http://dx.doi.org/10.1016/S0022-5096(99)00082-4.

[34] Miller R. Continuum plasticity model for the constitutive and indentation behaviour of foamed metals. Int J Mech Sci 2000;42:729–54. http://dx.doi.org/10.1016/S0020-7403(99)00021-1.

[35] Liu C, Huang Y, Stout M. On the asymmetric yield surface of plastically orthotropic materials: A phenomenological study. Acta Mater 1997;45(6):2397–406. http://dx.doi.org/10.1016/S1359-6454(96)00349-7.

[36] Drucker DC, Prager W. Soil mechanics and plastic analysis or limit design. Q Appl Math 1952;10(2):157–65. http://dx.doi.org/10.1090/qam/48291.

[37] Hill R. A theory of the yielding and plastic flow of anisotropic metals. Proc R Soc Lond Ser A Math Phys Eng Sci 1948;193(1033):281–97. http://dx.doi.org/10.1098/rspa.1948.0045.

[38] Salcedo-Sanz S, Rojo-Álvarez JL, Martínez-Ramón M, Camps-Valls G. Support vector machines in engineering: an overview. WIREs Data Min Knowl Discov 2014;4(3):234–67. http://dx.doi.org/10.1002/widm.1125.

[39] Bock FE, Aydin RC, Cyron CJ, Huber N, Kalidindi SR, Klusemann B. A review of the application of machine learning and data mining approaches in continuum materials mechanics. Front Mater 2019;6:1883. http://dx.doi.org/10.3389/fmats.2019.00110.

[40] Liu X, Tian S, Tao F, Yu W. A review of artificial neural networks in the constitutive modeling of composite materials. Composites B 2021;224:109152. http://dx.doi.org/10.1016/j.compositesb.2021.109152.

[41] Ibáñez R, Abisset-Chavanne E, González D, Duval J-L, Cueto E, Chinesta F. Hybrid constitutive modeling: data-driven learning of corrections to plasticity models. Int J Mater Form 2019;12(4):717–25. http://dx.doi.org/10.1007/s12289-018-1448-x.

[42] Frankel A, Hamel CM, Bolintineanu D, Long K, Kramer S. Machine learning constitutive models of elastomeric foams. Comput Methods Appl Mech Engrg 2022;391:114492. http://dx.doi.org/10.1016/j.cma.2021.114492.

[43] Heidenreich JN, Gorji MB, Mohr D. Modeling structure-property relationships with convolutional neural networks: Yield surface prediction based on microstructure images. Int J Plast 2023;163:103506. http://dx.doi.org/10.1016/j.ijplas.2022.103506.

[44] Shen W, Cao Y, Shao J, Liu Z. Prediction of plastic yield surface for porous materials by a machine learning approach. Mater Today Commun 2020;25:101477. http://dx.doi.org/10.1016/j.mtcomm.2020.101477.

[45] Settgast C, Hütter G, Kuna M, Abendroth M. A hybrid approach to simulate the homogenized irreversible elastic–plastic deformations and damage of foams by neural networks. Int J Plast 2020;126:102624. http://dx.doi.org/10.1016/j.ijplas.2019.11.003.

[46] Malik A, Abendroth M, Hütter G, Kiefer B. A hybrid approach employing neural networks to simulate the elasto–plastic deformation behavior of 3D-foam structures. Adv Energy Mater 2022;24(2):2100641. http://dx.doi.org/10.1002/adem.202100641.

[47] Fuhg JN, van Wees L, Obstalecki M, Shade P, Bouklas N, Kasemer M. Machine-learning convex and texture-dependent macroscopic yield from crystal plasticity simulations. Materialia 2022;23:101446. http://dx.doi.org/10.1016/j.mtla.2022.101446.

[48] Park H, Cho M. Multiscale constitutive model using data-driven yield function. Composites B 2021;216:108831. http://dx.doi.org/10.1016/j.compositesb.2021.108831.

[49] Mozaffar M, Bostanabad R, Chen W, Ehmann K, Cao J, Bessa MA. Deep learning predicts path-dependent plasticity. Proc Natl Acad Sci 2019;116(52):26414–20. http://dx.doi.org/10.1073/pnas.1911815116.

[50] Gorji MB, Mozaffar M, Heidenreich JN, Cao J, Mohr D. On the potential of recurrent neural networks for modeling path dependent plasticity. J Mech Phys Solids 2020;143:103972. http://dx.doi.org/10.1016/j.jmps.2020.103972.

[51] Bonatti C, Mohr D. On the importance of self-consistency in recurrent neural network models representing elasto-plastic solids. J Mech Phys Solids 2022;158:104697. http://dx.doi.org/10.1016/j.jmps.2021.104697.

[52] Liu X, He J, Huang S. Mechanistically informed artificial neural network model for discovering anisotropic path-dependent plasticity of metals. Mater Des 2023;226:111697. http://dx.doi.org/10.1016/j.matdes.2023.111697.

[53] Bomarito G, Townsend T, Stewart K, Esham K, Emery J, Hochhalter J. Development of interpretable, data-driven plasticity models with symbolic regression. Comput Struct 2021;252:106557. http://dx.doi.org/10.1016/j.compstruc.2021.106557.

[54] Hartmaier A. Data-oriented constitutive modeling of plasticity in metals. Materials 2020;13(7):1600. http://dx.doi.org/10.3390/ma13071600.

[55] Shoghi R, Hartmaier A. Optimal data-generation strategy for machine learning yield functions in anisotropic plasticity. Front Mater 2022;9:868248. http://dx.doi.org/10.3389/fmats.2022.868248.

[56] Flaschel M, Kumar S, De Lorenzis L. Discovering plasticity models without stress data. Npj Comput Mater 2022;8(1):1–10. http://dx.doi.org/10.1038/s41524-022-00752-4.

[57] Dassault Systèmes Simulia Corp. ABAQUS 2020 SE. 2020, Johnston, RI, USA.

[58] Hopcroft MA, Nix WD, Kenny TW. What is the Young's modulus of silicon? J Microelectromech Syst 2010;19(2):229–38. http://dx.doi.org/10.1109/JMEMS.2009.2039697.

[59] Lai W, Rubin D, Rubin D, Krempl E. Introduction to continuum mechanics. 4th ed.. Boston: Butterworth-Heinemann; 2010, http://dx.doi.org/10.1016/B978-0-7506-8560-3.X0001-1.

[60] Bergström J. 4 - continuum mechanics foundations. In: Bergström J, editor. Mech solid polym. William Andrew Publishing; 2015, p. 131–207. http://dx.doi.org/10.1016/B978-0-323-31150-2.00004-2.

[61] Muller ME. Some continuous Monte Carlo methods for the Dirichlet problem. Ann Math Stat 1956;27(3):569–89. http://dx.doi.org/10.1214/aoms/1177728169.

[62] Pedregosa F, Varoquaux G, Gramfort A, Michel V, Thirion B, Grisel O, Blondel M, Prettenhofer P, Weiss R, Dubourg V, Vanderplas J, Passos A, Cournapeau D, Brucher M, Perrot M, Duchesnay E. Scikit-learn: Machine learning in python. J Mach Learn Res 2011;12:2825–30. http://dx.doi.org/10.48550/arXiv.1201.0490.

[63] Buitinck L, Louppe G, Blondel M, Pedregosa F, Mueller A, Grisel O, Niculae V, Prettenhofer P, Gramfort A, Grobler J, Layton R, Vanderplas J, Joly A, Holt B, Varoquaux G. API design for machine learning software: experiences from the scikit-learn project. In: ECML PKDD workshop: Languages for data mining and machine learning. 2013, p. 108–22. http://dx.doi.org/10.48550/arXiv.1309.0238.

[64] Kecman V. Support vector machines – An introduction. In: Wang L, editor. Support vector machines: Theory and applications. Studies in fuzziness and soft computing, Berlin, Heidelberg: Springer; 2005, p. 1–47. http://dx.doi.org/10.1007/10984697_1.

[65] Farkas D, Caro A, Bringa E, Crowson D. Mechanical response of nanoporous gold. Acta Mater 2013;61(9):3249–56. http://dx.doi.org/10.1016/j.actamat.2013.02.013.

[66] Sun X-Y, Xu G-K, Li X, Feng X-Q, Gao H. Mechanical properties and scaling laws of nanoporous gold. J Appl Phys 2013;113(2):023505. http://dx.doi.org/10.1063/1.4774246.

[67] Bock FE, Keller S, Huber N, Klusemann B. Hybrid modelling by machine learning corrections of analytical model predictions towards high-fidelity simulation solutions. Materials 2021;14(8):1883. http://dx.doi.org/10.3390/ma14081883.